arXiv:1304.2413v1 [physics.atom-ph] 8 Apr 2013

1

Multielectron High Harmonic Generation: simple man on a complex plane

Olga Smirnova and Misha Ivanov

1.1
Introduction

Attosecond science has emerged with the discovery of coherent electron-ion collisions induced by a strong laser field, usually referred to as "re-collisions" (Corkum (1993)). This discovery was initiated by the numerical experiments of K. Schafer, J. Krause and K. Kulander (see Krause *et al.* (1992a)). The work by Corkum (1993) drew on the concepts developed in the earlier work of Brunel (1987, 1990) and Corkum *et al.* (1989). It has also been predated by the concept of the 'Atomic Antenna' (Kuchiev (1987)). With the benefit of hindsight, we now see the work by Kuchiev (1987) as the earliest quantum counterpart of the classical picture developed by Corkum (1993) and Kulander *et al.* (1993) [1].

The classical picture of strong-field-induced ionization dynamics is summarized as follows. Once ionization removes an electron from an atom or a molecule, this electron finds itself in the strong oscillating laser field. Newton's equations of motion show that, within one or few cycles after ionization, the oscillating electron can be driven back by the laser field to re-encounter the parent ion. During this re-encounter, referred to as re-collision, the electron can do many things: scatter elastically (diffract), scatter inelastically (excitation or ionization of the parent ion), or radiatively recombine into one of the ion's empty states. It is this latter process that we will focus on here. The classical picture is usually referred to as the three-step model, or the simple man model [2].

If the recombination occurs to the exact same state that the electron has left from,

---

1) While the quantum vision of Kuchiev (1987) has predated the classical picture, at that time it lacked the striking clarity and transparency of the classical model (Corkum (1993)), which linked several key – and seemingly disparate strong-field phenomena – high harmonic generation, production of very high energy electrons, and extreme efficiency of double ionization. The history of this discovery is rich and interesting in its own right. Some of it is recounted, from a more historical perspective, in Chapter 4. Our purpose here is different – we simply urge our reader to read the papers by Brunel (1987, 1990), Corkum *et al.* (1989), Kuchiev (1987), Schafer *et al.* (1993), as well as a seemingly unrelated paper of Gallagher (1988).

2) As far as one of us (M.I.) can remember, the latter term has been used by K. Kulander, K. Schafer and H.-G. Muller, who have contributed a lot to the development of this classical model.

2

then the phase of the emitted radiation is the same from one atom to another, leading to the generation of coherent radiation in the medium. This process is known as high harmonic generation (HHG). It produces tens of eV-broad coherent spectra and has two crucial applications. First, high harmonic emission is used to generate attosecond pulses of light (see e.g. Krausz and Ivanov (2009)), which can then be used in time-resolved pump-probe experiments. Second, the ultra-broad coherent harmonic spectrum carries attosecond information about the underlying nonlinear response, which can be extracted. The second direction is the subject of high harmonic spectroscopy (see e.g. Lein (2005); Baker *et al.* (2006); Smirnova *et al.* (2009a); Haessler *et al.* (2010)) – a new imaging technique with a combination of sub-Angstrom spatial and attosecond temporal resolution.

In the language of nonlinear optics, high harmonic generation is a frequency up-conversion process that results from the macroscopic response of the medium. The nonlinear polarization is induced in the medium by (i) the response of the atoms and the molecules, (ii) the response of the free electrons, (iii) the response of the guiding medium. Here we focus on the theory of single atom or single molecule response. The description of macroscopic propagation effects, which determine how coherent radiation from different atoms or molecules add together, can be found in Gaarde *et al.* (2008).

From the famous simple man model to the recent multichannel model, we will try to guide you through the several landmarks in our understanding of high harmonic generation. We hope to provide recipes and insight for modelling the harmonic response in complex systems. The chapter includes the following sections:

- 1.2 The **simple man model** of high harmonic generation (HHG);
- 1.3 Formal approach for one-electron systems;
- 1.4 **The Lewenstein model**: stationary phase equations for HHG;
- 1.5 Analysis of complex trajectories;
- 1.6 Factorization of the HHG dipole: simple man on a complex plane;
- 1.7 **The photoelectron model** of HHG: the improved 'simple man';
- 1.8 **The multichannel model** of HHG: Tackling multi-electron systems;
- 1.9 Outlook;
- 1.10 Acknowledgements;
- 1.11 Appendix A: Supplementary derivations;
- 1.12 Appendix B: The saddle point method;
- 1.13 Appendix C: Treating the cut-off region: regularization of the divergent stationary phase solutions;
- 1.14 Appendix D: Finding saddle points for the Lewenstein model.

Atomic units $\hbar = m = e = 1$ are used everywhere, unless specified otherwise.

1.2
The simple man model of high harmonic generation (HHG)

Experiments in the eighties and the early nineties of the last century yielded an as-tounding result: shaken with sufficiently intense infrared laser radiation, the atomic medium was found to up-convert the frequency of the driving infrared laser light by up to two orders of magnitude (see e.g. Huillier and Balcou (1993); Macklin *et al.* (1993)). The observed harmonic spectrum formed a long plateau, with many har-monic orders, followed by a sharp cut-off. This observation has to be placed in the context of what has been routinely seen in the traditional nonlinear optics: in the absence of resonances, the nonlinear response would decrease dramatically with in-creasing harmonic order, and the harmonic numbers would hardly ever reach double digits, let alone form a plateau extending beyond N=101.

To generate very high harmonics of the driving frequency, the atom has to ab-sorb lots of photons. Generation of harmonics with numbers like N=21,...,31,..., etc. means that at least that many photons (21, ..., 31, ...) had to be absorbed by the atom.

The minimal amount of photons required for ionization is $N_0 = I_p/\omega$, where I_p is the ionization potential and ω is the infrared laser frequency. For $I_p \sim 12-15$ eV and an 800 nm driving IR laser field (the standard workhorse in many HHG experiments), $N_0 \sim 10$. One would have thought that once ten or so photons are absorbed, the electron should be free. And since it is well-known that a free electron should not absorb any more photons, the emission should stop around $N = 11$ or so, in stark contrast with experimental observations.

Why and how many additional photons are absorbed? What is the underlying mechanism? The liberated electron oscillates in the laser field, and its instantaneous energy can be very high. Can this instantaneous electron energy be converted into the harmonic photons? Where is the source of non-linearity, if the free electron oscillates with the frequency of the laser field?

The physical picture that clearly answered these questions is the classical three-step model. It is simple, remarkably accurate, and is also intrinsically sub-cycle: within one optical period, an electron is (i) removed from an atom or molecule, (ii) accel-erated by the oscillating laser field, and (iii) driven back to re-collide with the parent ion. This picture connects the key strong-field phenomena: above-threshold ioniza-tion, non-sequential double ionization, and high harmonic generation. It reveals the source of non-linearity in HHG: the recombination of the accelerated electron with the ion.

How can one check that this mechanism is indeed responsible for HHG? The key thing test is whether or not this picture explains the cut-off of the harmonic spectra, that is, the highest harmonic order that can be efficiently produced. Numerically, the empirical cut-off law was found to be $\Omega_{\max} = I_p + 3U_p$ (Krause *et al.* (1992b)), where U_p is the cycle-averaged energy of the electron's oscillatory motion in the laser field. To calculate the classical cut-off, we should calculate the maximal instantaneous en-ergy of the returning electron, but to do so we need to know the initial conditions for the electron just after ionization. These conditions are specified within the three-step (simple man) model of HHG, which makes the following assumptions:
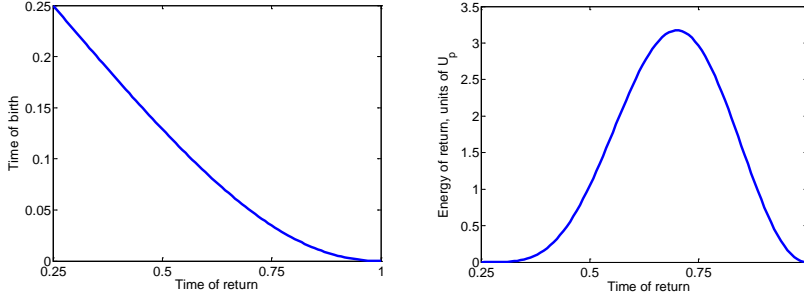
4

Figure 1.1 Window of classical 'birth' times and the return energy. Left panel: Time of birth vs. time of return. Right panel: Energy of the electron at the time of return.

- SM1: The electron is born in the continuum at any time within the laser cycle;
- SM2: The electron is born near the ionic core (i.e., near the origin of the reference frame) with zero velocity;
- SM3: If the electron returns to the ionic core (origin), its instantaneous energy at the moment of return is converted into the harmonic photon.

The pull of the ionic core on the liberated electron is neglected in the model, which is not unreasonable considering the very large excursions that the electron makes in the strong driving laser field. The possibility of the electrons return to the core is dictated by the phase of the laser field at which it is launched on its classical orbit, and the time-window for the returning trajectories – the range of the 'birth' times t_B – shown in Fig. 1.1.

The calculation is done as follows: for each t_B, we find the time of return t_R to the electron's original position (Fig. 1.1, left panel) and the energy at the moment of return (Fig. 1.1, right panel). The assumption that the strong laser field dominates the electron's motion after ionization simplifies our calculations. Once the ionic core potential is neglected, the kinetic momentum (velocity) at the time of birth t_B can be written as $\mathbf{k}(t_B) = \mathbf{p} + \mathbf{A}(t_B)$, where $\mathbf{p}$ is the canonical momentum of the electron and $\mathbf{A}(t)$ is the vector potential of the laser field, which is related to the electric field $\mathbf{F}(t)$ as $\mathbf{F}(t) = -\partial \mathbf{A}/\partial t$. The condition $\mathbf{k}(t_B) = \mathbf{0}$ (SM2) specifies $\mathbf{p} = -\mathbf{A}(t_B)$. Therefore, the electron kinetic momentum at all later times t is $\mathbf{k}(t) = -\mathbf{A}(t_B) + \mathbf{A}(t)$ and the electron energy at the time of return is

$$E_{\mathrm{ret}}(t_R) = \mathbf{k}^2(t_R)/2 = (\mathbf{A}(t_B) - \mathbf{A}(t_R))^2/2 .$$

The zero displacement of the electron from the time of birth, t_B, to the time of return, t_R, (SM3) defines the return time t_R:

$$\int_{t_B}^{t_R} dt\, (\mathbf{A}(t) - \mathbf{A}(t_B)) = 0. \tag{1.1}$$

According to this model, the maximal return energy is about 3.17 U_p, where $U_p = F^2/4\omega^2$ and F is the electric field amplitude (see Fig. 1.1). Then the maximum

energy of the emitted harmonic photon is $3.17\,U_p + I_p$, where I_p is the binding energy of the ground state to which the electron recombines, is in excellent agreement with the empirical cut-off law found numerically by Krause *et al.* (1992a).

The formal quantum approach considered in the next section will first take us away from the simple classical model. However, just like the re-colliding electron revisits the ion, we will revisit the simple man model several times in this chapter, refining it at each step.

1.3
Formal approach for one-electron systems

The response of an individual atom or a molecule $\mathbf{P}(\mathbf{r}, t) = n\mathbf{D}(t)$ is proportional to the induced dipole $\mathbf{D}(t)$:

$$\mathbf{D}(t) = \langle \Psi(t)|\hat{\mathbf{d}}|\Psi(t)\rangle, \tag{1.2}$$

where n is the number density, $\hat{\mathbf{d}}$ is the dipole operator, and $\Psi(t)$ is the wavefunction of the system obtained by solving the time-dependent Schrödinger equation (TDSE) with the Hamiltonian $\hat{H}(t)$:

$$i\partial\Psi(t)/\partial t = \hat{H}(t)\Psi(t). \tag{1.3}$$

We will first focus on the single-active-electron approximation (see section 1.8 for the multielectron case). This approximation assumes that only one electron feels the laser field – the one that is liberated via strong-field ionization and subsequently re-collides with the parent ion. All other electrons are frozen in the ion, unaffected by the laser field. The Hamiltonian of our system in the single-active-electron approximation is

$$\hat{H}(t) = \hat{\mathbf{p}}^2/2 + U(\hat{\mathbf{r}}) + \hat{V}_L(t), \tag{1.4}$$

where $\hat{\mathbf{p}} = -i\nabla_{\mathbf{r}}$ is the momentum operator, $U(\hat{\mathbf{r}})$ describes the interaction of the electron with the ionic core, and $\hat{V}_L(t)$ describes the interaction between the electron and the laser field. In the dipole approximation and in the length gauge, $\hat{V}_L(t) = -\hat{\mathbf{d}} \cdot \mathbf{F}(t) = \hat{\mathbf{r}} \cdot \mathbf{F}(t)$ (see Chapter 8 to learn about different gauges or read Section 2.2.4 in the excellent book by Grynberg *et al.* (2010) for a more detailed discussion).

Formally, the solution of the Schrödinger equation (1.3) can be written in the integral form (see e.g. Smirnova *et al.* (2007b) for a simple derivation):

$$|\Psi(t)\rangle = -i \int_{t_0}^{t} dt' \, \hat{U}(t, t')\hat{V}_L(t')\hat{U}_0(t', t_0)|g\rangle + \hat{U}_0(t, t_0)|g\rangle, \tag{1.5}$$

where the ket-vector $|g\rangle$ represents the wavefunction of the electron in the ground state at initial time $t = t_0$, $\hat{U}(t, t')$ is the full propagator, while $\hat{U}_0(t', t_0)$ is the field-free propagator. The propagators are the operators that describe the time evolution of the wavefunction. The propagator $\hat{U}_0(t', t_0)$ governs the electron dynamics from

time t_0 to time t' without the laser field, and is determined by the following equations:

$$i\partial \hat{U}_0(t, t_0)/\partial t = \hat{H}_0 \hat{U}_0(t, t_0), \tag{1.6}$$

$$\hat{U}_0(t_0, t_0) = 1, \tag{1.7}$$

$$\hat{H}_0 = \hat{\mathbf{p}}^2/2 + U(\hat{\mathbf{r}}). \tag{1.8}$$

Symbolically, the solution of Eq. (1.6) can be written in the compact form

$$\hat{U}_0(t', t_0) = e^{-i\int_{t_0}^{t'} \hat{H}_0(\xi)\, d\xi}, \tag{1.9}$$

where the integral is *time-ordered*, that is, the contribution of later times to the evolution follows the contribution of the earlier times.

The full propagator $\hat{U}(t, t')$ governs the electron dynamics from time t' to the observation time t, driven by the combined action of the laser field and of the ionic core potential $U(\hat{\mathbf{r}})$. It is given by

$$i\partial \hat{U}(t, t')/\partial t = \hat{H}\hat{U}(t, t'), \tag{1.10}$$

$$\hat{U}(t, t') = e^{-i\int_{t'}^{t} \hat{H}(\xi)\, d\xi}, \tag{1.11}$$

$$\hat{U}(t', t') = 1. \tag{1.12}$$

The propagation without the laser field is straightforward. Denoting the ground state energy $E_g = -I_p$ (ionization potential) and the stationary ground state wavefunction $\Psi_g(\mathbf{r}) = \langle \mathbf{r}|g\rangle$, we have:

$$\Psi_g(\mathbf{r}, t') = U_0(t', t_0)\Psi_g(\mathbf{r}) = e^{iI_p(t'-t_0)}\Psi_g(\mathbf{r}). \tag{1.13}$$

The full propagator $\hat{U}(t, t')$, on the other hand, is just as hard to find as the solution of the original equation (1.3). The advantage of the integral expression Eq. (1.5) is that making meaningful approximations is technically easier and physically more transparent.

Remembering that the laser field is strong, we can try to neglect the ionic potential in the full propagator. In this case the electron is free from time t' to time t. Its motion is only affected by the laser field and is described by the Hamiltonian $\hat{H}_V(t) = \hat{\mathbf{p}}^2/2 + \hat{V}_L(t)$. The corresponding approximation is called the Strong Field Approximation (SFA), and the propagator corresponding to $\hat{H}_V(t)$ is often called the Volkov propagator. The main advantage of the SFA is that the Volkov propagator can be found analytically.In the length gauge used here, the result of acting with the Volkov propagator $\hat{U}_V(t, t')$ on the plane wave with kinetic momentum $\mathbf{k}(t') = \mathbf{p} + \mathbf{A}(t')$ is

$$\hat{U}_V(t, t')|\mathbf{p} + \mathbf{A}(t')\rangle = e^{-iS_V(\mathbf{p}, t, t')}|\mathbf{p} + \mathbf{A}(t)\rangle,$$

$$\langle \mathbf{r}|\mathbf{p} + \mathbf{A}(t)\rangle = \frac{1}{(2\pi)^{3/2}}e^{i[\mathbf{p}+\mathbf{A}(t)]\cdot \mathbf{r}},$$

$$S_V(\mathbf{p}, t, t') = \frac{1}{2}\int_{t'}^{t} d\xi\,[\mathbf{p} + \mathbf{A}(\xi)]^2. \tag{1.14}$$

That is, the plane wave with the kinetic momentum $\mathbf{k}(t') = \mathbf{p} + \mathbf{A}(t')$ turns into a plane wave with the kinetic momentum $\mathbf{k}(t) = \mathbf{p} + \mathbf{A}(t)$ and accumulates the phase $S_V(\mathbf{p}, t, t')$ on the way.

The Eqs. (1.14) define the Volkov function

$$\Psi_{\mathbf{p}}^V(\mathbf{r}, t; t') = \frac{1}{(2\pi)^{3/2}} e^{-iS_V(\mathbf{p}, t, t')} e^{i[\mathbf{p} + \mathbf{A}(t)] \cdot \mathbf{r}} \quad .$$

Formally, the Volkov function is an eigenstate of the time-periodic Hamiltonian. It provides the quantum-mechanical description of the behavior of the free electron in the laser field. The coordinate part of the Volkov function is a plane wave, and these plane waves form a complete basis at each moment of time:

$$\hat{1} = \int d\mathbf{p} \, |\mathbf{p} + \mathbf{A}(t)\rangle \langle \mathbf{p} + \mathbf{A}(t)|. \tag{1.15}$$

Within the SFA, Eq.(1.5) takes the form

$$|\Psi(t)\rangle = -i \int_{t_0}^{t} dt' \, \hat{U}_V(t, t') \hat{V}_L(t') \hat{U}_0(t', t_0) |g\rangle + \hat{U}_0(t, t_0) |g\rangle, \tag{1.16}$$

and can be solved analytically. The first term describes ionization, the second term describes the evolution of the non-ionized part of the electron wavefunction.

Thus, it is natural to associate t' with the time when ionization is initiated: before t' the electron is bound, after t' the electron is becoming free. Substituting Eq. (1.16) into Eq. (1.2) yields:

$$\mathbf{D}(t) \simeq -i \langle \hat{U}_0(t, t_0) g | \hat{\mathbf{d}} | \int_{t_0}^{t} dt' \, \hat{U}_V(t, t') \hat{V}_L(t') \hat{U}_0(t', t_0) |g\rangle + c.c. \tag{1.17}$$

Here we have assumed that there is no permanent dipole in the ground state and that the contribution of the continuum-continuum transitions to the dipole is negligible. The latter assumption is fine as long as ionization is weak. Thus, the dipole in Eq. (1.17) is evaluated between the bound and the continuum components of the same wavefunction.

The propagator $\hat{U}_V(t, t')$ is known when it acts on the Volkov states. Thus, we introduce the identity operator resolved on the Volkov states, Eq. (1.15), into Eq. (1.17):

$$\mathbf{D}(t) = -i \langle g | \hat{\mathbf{d}} | \int_{t_0}^{t} dt' \, e^{iI_p(t'-t)} \times$$
$$\times \int d\mathbf{p} \, U_V(t, t') |\mathbf{p} + \mathbf{A}(t')\rangle \langle \mathbf{p} + \mathbf{A}(t') | \hat{V}_L(t') |g\rangle + c.c. \quad . \tag{1.18}$$

Finally, remembering that $\hat{V}_L(t) = -\hat{\mathbf{d}} \cdot \mathbf{F}(t)$, we re-write Eq. (1.18) in the compact form:

$$\mathbf{D}(t) = i \int_{t_0}^{t} dt' \int d\mathbf{p} \, \mathbf{d}^*(\mathbf{p} + \mathbf{A}(t)) \, e^{-iS(\mathbf{p}, t, t')} \, \mathbf{F}(t') \, \mathbf{d}(\mathbf{p} + \mathbf{A}(t')) + c.c., \tag{1.19}$$

where we have introduced the dipole matrix elements $\mathbf{d}(\mathbf{p} + \mathbf{A}(t))$ of the transitions between the ground state and the plane wave continuum,

$$\mathbf{d}(\mathbf{p} + \mathbf{A}(t)) \equiv \langle \mathbf{p} + \mathbf{A}(t) | \hat{\mathbf{d}} | g \rangle. \tag{1.20}$$

The phase

$$S(\mathbf{p}, t, t') \equiv \frac{1}{2} \int_{t'}^{t} [\mathbf{p} + \mathbf{A}(\tau)]^2 d\tau + I_p(t - t') \qquad (1.21)$$

is often referred to as action, and we will use this term below, even though, strictly speaking, it is only the energy part of the full classical action.

It is convenient to re-write the equation (1.19) for the harmonic dipole $\mathbf{D}(t)$ by evaluating the integral over t' by parts (see e.g. Gribakin and Kuchiev (1997), Becker *et al.* (2002b) and Appendix A):

$$\int_{t_0}^{t} dt' \, e^{-iS(\mathbf{p}, t, t')} \, \mathbf{F}(t') \, \mathbf{d}(\mathbf{p} + \mathbf{A}(t')) = \qquad (1.22)$$

$$= \int_{t_0}^{t} dt' \, e^{-iS(\mathbf{p}, t, t')} \Upsilon(\mathbf{p} + \mathbf{A}(t')),$$

$$\Upsilon(\mathbf{p} + \mathbf{A}(t')) = \left[\frac{(\mathbf{p} + \mathbf{A}(t'))^2}{2} + I_p \right] \langle \mathbf{p} + \mathbf{A}(t') | g \rangle, \qquad (1.23)$$

where $\langle \mathbf{p} + \mathbf{A}(t) | g \rangle$ is a Fourier transform of the ground state $|g\rangle$, $\Upsilon(\mathbf{p})$ reflects the dependence of ionization rate on the angular structure of the ground state. Equation (1.19) takes the following form:

$$\mathbf{D}(t) = i \int_{t_0}^{t} dt' \int d\mathbf{p} \, \mathbf{d}^*(\mathbf{p} + \mathbf{A}(t)) \, e^{-iS(\mathbf{p}, t, t')} \Upsilon(\mathbf{p} + \mathbf{A}(t')) + c.c., \qquad (1.24)$$

The harmonic spectrum $I(N\omega)$ can be obtained from the Fourier transform of $\mathbf{D}(t)$:

$$I(N\omega) \propto (N\omega)^4 |D(N\omega)|^2,$$

$$\mathbf{D}(N\omega) = \int dt \, e^{iN\omega t} \, \mathbf{D}(t). \qquad (1.25)$$

Note that $S(\mathbf{p}, t, t')$ is large and the integrand is a highly oscillating function, which is an advantage for the analytical evaluation of this integral. The analytical approach (Lewenstein *et al.* (1994)) is based on the saddle point method (see Appendix B), which is the mathematical tool for evaluating integrals from fast-oscillating functions. It provides the physical picture of high harmonic generation as a three step process involving ionization, propagation and recombination (Ivanov *et al.* (1996)). It also supplies the time-energy mapping (Lein (2005); Baker *et al.* (2006)) crucial for attosecond imaging, and it is the basis for the extension of the above approach beyond the SFA and beyond the single-active-electron approximation (see e.g. Smirnova *et al.* (2009a)).

Let us now focus on the analytical saddle point approach to HHG.

1.4
The Lewenstein model: Saddle point equations for HHG

The goal of this section is to evaluate the integral equations (1.24,1.25) using the saddle point method (see Appendix B). We need to find saddle points for all three integration variables t', t and $\mathbf{p}$, i.e. points where the rapidly changing phase of the integrand has zero derivatives with respect to all integration variables.

There are two ways to deal with the integrals Eqs. (1.24,1.25). First, one can treat them as multi-dimensional integral, i.e. one finds the saddle points for all the integration variables 'in parallel', and then one follows the multi-dimensional saddle point approach to deal with the whole multi-dimensional integral 'at once'.

One can also take a different route and evaluate the multiple integrals (1.24,1.25) step by step, sequentially. First, we find the saddle points t_i for the integral over t' from the saddle point equation:

$$\frac{dS}{dt'} \equiv \frac{\partial S(t', \mathbf{p}, t)}{\partial t'} = 0, \tag{1.26}$$

where the phase S is given by Eq. (1.21). We then evaluate the integral over t' treating it as a one-dimensional integral, with $\mathbf{p}$ and t entering as fixed parameters.

Next, we move to the integral over $\mathbf{p}$. Dealing with its saddle points, we should keep in mind that the saddle points of the previous integral $t' = t_i \equiv t_i(\mathbf{p}, t)$ depend on $\mathbf{p}$: $\frac{\partial t_i}{\partial p_\alpha} \neq 0$, $\alpha = x, y, z$.

Fortunately, thanks to Eq. (1.26), the explicit dependence of $t_i(\mathbf{p}, t)$ on $\mathbf{p}$ does not affect the position of the saddle points for the $\mathbf{p}$-integral:

$$\frac{dS(t_i, \mathbf{p}, t)}{dp_\alpha} \equiv \frac{\partial S(t_i, \mathbf{p}, t)}{\partial p_\alpha} + \frac{\partial S(t_i, \mathbf{p}, t)}{\partial t_i}\frac{dt_i}{dp_\alpha} = \frac{\partial S(t_i, \mathbf{p}, t)}{\partial p_\alpha} = 0. \tag{1.27}$$

Note that the integral over $\mathbf{p}$ is multi-dimensional, which leads to a slightly different form of the pre-exponential factor (prefactor) involving Hessian(see Appendix B).

Finally, we deal with the integral over t. Here, again, the saddle points $\mathbf{p}_s(t_i, t)$ depend on t: $\frac{\partial p_{s,\alpha}}{\partial t} \neq 0$. But once again the explicit dependence of $\mathbf{p}_s(t_i, t)$ on t does not affect the position of the saddle points thanks to Eq. (1.27):

$$\frac{dS(t_i, \mathbf{p}_s, t)}{dt} \equiv \frac{\partial S(t_i, \mathbf{p}_s, t)}{\partial t} + \frac{\partial S(t_i, \mathbf{p}_s, t)}{\partial p_\alpha}\frac{dp_\alpha}{dt} = \frac{\partial S(t_i, \mathbf{p}_s, t)}{\partial t} = 0. \tag{1.28}$$

The fact that both routes yield the same saddle point equations is, of course, not surprising – one should not get different answers depending on how the integral is evaluated.

Using Eq. (1.21), we obtain the explicit form of the Eqs. (1.26,1.27,1.28), which define the saddle points t_i, $\mathbf{p}_s$, t_r:

$$\frac{[\mathbf{p}_s + \mathbf{A}(t_i)]^2}{2} + I_p = 0, \tag{1.29}$$

$$\int_{t_i}^{t_r} [\mathbf{p}_s + \mathbf{A}(t')]\, dt' = 0, \tag{1.30}$$

$$\frac{[\mathbf{p}_s + \mathbf{A}(t_r)]^2}{2} + I_p = N\omega. \tag{1.31}$$
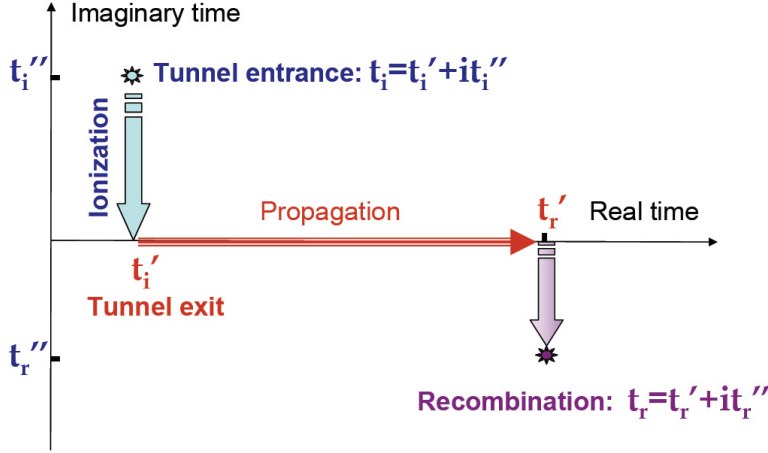
Figure 1.2 Contour of the time integration in the action S. Ionization occurs from the complex time t_i to the real time t_i'.

Here, $\mathbf{p}_s$ is the electron drift (canonical) momentum, $\mathbf{k}_s(t) = \mathbf{p}_s + \mathbf{A}(t)$ is the kinetic momentum (the instantaneous electron velocity, up to the electron mass). The trajectories that satisfy the Eqs. (1.29,1.30,1.31) are known as quantum orbits, see Salieres *et al.* (2001), Kopold *et al.* (2002), Becker *et al.* (2002a).

Equation (1.30) requires that the electron returns to the parent ion – the prerequisite for recombination. Indeed, the time integral of the electron velocity yields the electron displacement from t_i to t_r. Thus, Eq. (1.30) dictates that the displacement is equal to zero.

Whereas Eq. (1.31) describes energy conservation during recombination, Eq. (1.29) describes tunnelling. It shows that the electron's kinetic energy at t_i is negative, its velocity $\mathbf{k}_s(t_i) = \mathbf{p}_s + \mathbf{A}(t_i)$ is complex, and hence $t_i = t_i' + t_i''$ is also complex – the hallmarks of the tunnelling process.

The time t_i can be identified with the moment when the electron *enters the barrier*, see Fig. 1.2. Its *real part* will then correspond to the time when the electron *exits the barrier*. The origin of this concept will be explained in the next section.

The electron displacement during this 'under-the-barrier' motion from t_i to $\mathrm{Re}(t_i)$ is, in general, complex. Whether we like it or not, it yields a complex coordinate of 'exit' $\mathbf{r}_{ex} = \mathbf{r}_{ex}' + i\mathbf{r}_{ex}''$ at $\mathrm{Re}(t_i) \equiv t_i'$ (see e.g. Torlina and Smirnova (2012)):

$$\int_{t_i}^{t_i'} [\mathbf{p} + \mathbf{A}(t')]dt' = \mathbf{r}_{ex}' + i\mathbf{r}_{ex}''. \tag{1.32}$$

As a result, Eqs. (1.30) and (1.31) cannot be satisfied unless $\mathbf{p}$ or t_r are complex. Indeed, t_r must be complex to compensate for the imaginary displacement accumulated under the barrier. However, the energy conservation condition in Eq. (1.31) dictates that $\mathbf{k}_s(t_r) = \mathbf{p}_s + \mathbf{A}(t_r)$ is real at the moment of recombination. Therefore $\mathbf{p}_s$ must also be complex to compensate for the imaginary part of $\mathbf{A}(t_r)$.

Thus, we are forced to conclude that, in contrast to the classical trajectories of the simple man model, the quantum orbits are the trajectories with complex canonical momenta, complex velocities, and complex displacements. These trajectories evolve in complex time. The only quantity that is required to be real is the one we measure – the energy of the emitted photon, see Eq. (1.31). Later in this chapter, we will see when and how one can replace these trajectories with a different set of trajectories that do not involve complex canonical momenta and therefore better correspond to the classical picture. But for the moment, let us deal with the problem at hand.

For a linearly polarized field, it is convenient to rewrite the Eqs. (1.29,1.30,1.31) in terms of electron momenta parallel, $p_{s,\parallel}$, and perpendicular, $p_{s,\perp}$, to the polarization vector of the laser field:

$$\frac{[p_{s,\parallel} + A(t_i)]^2}{2} + I_{p,\text{eff}} = 0, \tag{1.33}$$

$$\int_{t_i}^{t_r} [p_{s,\parallel} + A(t')]\, dt' = 0, \qquad \int_{t_i}^{t_r} p_{s,\perp}\, dt' = 0, \tag{1.34}$$

$$\frac{[p_{s,\parallel} + A(t_r)]^2}{2} + I_{p,\text{eff}} = N\omega, \tag{1.35}$$

where we have introduced an "effective" ionization potential: $I_{p,\text{eff}} = I_p + p_{s,\perp}^2/2$. Equations (1.34) dictate that the stationary perpendicular canonical momentum is equal to zero for the linearly polarized field, $p_{s,\perp} = 0$ and hence $I_{p,\text{eff}} = I_p$. Then, Eqs. (1.33,1.34,1.35) reduce to:

$$\frac{[p_{s,\parallel} + A(t_i)]^2}{2} + I_p = 0, \tag{1.36}$$

$$\int_{t_i}^{t_r} [p_{s,\parallel} + A(t')]\, dt' = 0, \tag{1.37}$$

$$\frac{[p_{s,\parallel} + A(t_r)]^2}{2} + I_p = N\omega. \tag{1.38}$$

Separating the real and the imaginary parts in Eqs. (1.36, 1.37, 1.38), we obtain six equations for six unknowns: $t_i = t_i' + it_i''$, $t_r = t_r' + it_r''$, $p_{s,\parallel} = p' + ip''$. Our goal is to solve these equations for each harmonic order N. Here is one way to do it, which we find simple and visually appealing.

First, we use the Eqs. (1.36,1.38) to express all variables via the real, t_r', and the imaginary, t_r'', return times. This can be done analytically. Second, we substitute the result into the real part and the imaginary part of Eq. (1.37):

$$F_1(N, t_r', t_r'') = \text{Re}\left[\int_{t_i}^{t_r} [p_{s,\parallel} + A(t')]dt'\right] = 0, \tag{1.39}$$

$$F_2(N, t_r', t_r'') = \text{Im}\left[\int_{t_i}^{t_r} [p_{s,\parallel} + A(t')]dt'\right] = 0. \tag{1.40}$$

Third, we solve the Eqs. (1.39,1.40) to find the only two remaining unknowns: the real, t_r', and the imaginary, t_r'', return times. While the Eqs. (1.39,1.40) cannot be

solved analytically, dealing with two equations is much easier than dealing with the original six.

Solving the Eqs. (1.39,1.40) means that we need to find the minima of the two-dimensional surface $F(N, t'_r, t''_r)$, defined in the plane of the real, t'_r, and the imaginary, t''_r, return times:

$$F(N, t'_r, t''_r) \equiv [F_1(N, t'_r, t''_r)]^2 + [F_2(N, t'_r, t''_r)]^2 = 0. \tag{1.41}$$

These minima can be easily found numerically using the gradient method. The advantage of using $F(N, t'_r, t''_r)$ is the ability to visualize the solutions: by simply plotting the surface given by Eq. (1.41), see Fig. 1.3, one can examine the positions of the minima versus the harmonic number N.

If we restrict our analysis to those solutions that lie within the same cycle of the laser field as the moment of ionization, $\mathrm{Re}(t_i)$, we will find two stationary solutions for each harmonic number N. These solutions are discussed in detail in the next section. They correspond to two families of quantum orbits, called the 'short' and the 'long' trajectories. The trajectories merge for the largest possible return energies, i.e. near the cut-off of the harmonic spectrum.

There are also solutions that lie outside the laser cycle during which the electron was 'born' into the continuum. These 'super-long' trajectories describe second, third, and higher-order returns of the electron to the origin. In typical experimental conditions, their contribution to the high harmonic emission is negligible thanks to the macroscopic effects – very long trajectories do not phase match well (see e.g. Salieres *et al.* (2001)). Only very recently, the beautiful experiments of Zair *et al.* (2008) have been able to clearly resolve the contribution of these trajectories, and even identify their interference with the contribution from the long and the short trajectories.

The stationary phase method for the integral over the return time t breaks down when these two stationary points merge and the second derivative of the action with respect to the return time is equal to zero, $\partial^2 S / \partial t^2 = 0$. At this point, one needs to replace the standard saddle point method with the regularization procedure, discussed in Appendix C.

Outside the cut-off region, and up to a global phase factor, the saddle point method yields the following expression for the harmonic dipole (1.24,1.25):

$$\mathbf{D}(N\omega) = \sum_{j=1}^{4M} \left[\frac{2\pi}{iS''_{t_i,t_i}} \right]^{\frac{1}{2}} \left[\frac{2\pi}{iS''_{t_r,t_r}} \right]^{\frac{1}{2}} \frac{(2\pi)^{3/2}}{\sqrt{\det(iS''_{\mathbf{p}_s,\mathbf{p}_s})}} \times$$

$$\times \mathbf{d}^*(\mathbf{p}_s + \mathbf{A}(t_r^{(j)}))\, e^{-iS(\mathbf{p}_s, t_r^{(j)}, t_i^{(j)})}\, \Upsilon(\mathbf{p}_s + \mathbf{A}(t_i))\, e^{iN\omega t_r^{(j)}}, \tag{1.42}$$

where the Hessian $\det(iS''_{\mathbf{p}_s,\mathbf{p}_s})$ appears due to the multi-dimensional nature of the integral over $\mathbf{p}$. The sum runs over all stationary points j for M periods of the laser light, and the corresponding ionization and recombination times are labelled with the superscript j. Since there are two trajectories for each half-cycle of the laser field, i.e. for each ionization 'burst', and since there are 2M ionization bursts for M laser cycles, the number of stationary points is $4M$.

The length gauge SFA presents a good approximation for short range potentials

Frolov *et al.* (2003). However, it misses polarization, the Stark shift and the depletion of the bound state, which can be introduced into Eq. (1.42) if necessary.

Note that the expression (1.42) **can not** be directly ported to long range potentials. Indeed, in the long range Coulomb potential the ground state has different radial structure (compare Eqs.(1.55) and (1.56) below) and $\Upsilon(\mathbf{p}_s + \mathbf{A}(t_i))$ is singular exactly at the saddle point $[\mathbf{p}_s + \mathbf{A}(t_i)]^2/2 + I_p = 0$. As a consequence, the saddle point calculations should be modified, (see e.g. Keldysh (1965); Gribakin and Kuchiev (1997)) to accommodate for the presence of such singularity. Once the singularity is treated correctly (Keldysh (1965); Gribakin and Kuchiev (1997)), the result is still incomplete and unsatisfactory, because the long range potential also affects the structure of the continuum states, which can not be accurately represented by the Volkov states. Consistent treatment of long-range effects including modifications of both bound and continuum states can be found in Torlina and Smirnova (2012); Kaushal and Smirnova (2013). A practical recipe for incorporating the effects of the Coulomb potential is discussed in the next section and in the Outlook section.

1.5
Analysis of the complex trajectories

Let us now show how the above method of finding the saddle points works for a linearly polarized laser field $F = F_0 \cos(\omega t)$, which corresponds to the vector potential $A = -A_0 \sin(\omega t)$. We shall introduce the dimensionless variables $p_1 = \mathrm{Re}(p_{s,\parallel})/A_0$, $p_2 = \mathrm{Im}(p_{s,\parallel})/A_0$, $\phi_i = \omega t_i = \phi_i' + i\phi_i''$, $\phi_r = \omega t_r = \phi_r' + i\phi_r''$, $\gamma^2 = I_p/(2U_p)$, $\gamma_N^2 = (N\omega - I_p)/(2U_p)$.

In terms of these variables, Eqs. (1.39,1.40) for the linearly polarized field yield:

$$
\begin{aligned}
F_1 &= p_1(\phi_r' - \phi_i') - p_2(\phi_r'' - \phi_i'') - \cos(\phi_i')\cosh(\phi_i'') \\
&\quad + \cosh(\phi_r'')\cos(\phi_r') = 0, \tag{1.43}
\end{aligned}
$$

$$
\begin{aligned}
F_2 &= p_1(\phi_r'' - \phi_i'') + p_2(\phi_r' - \phi_i') + \sin(\phi_i')\sinh(\phi_i'') \\
&\quad - \sinh(\phi_r'')\sin(\phi_r') = 0. \tag{1.44}
\end{aligned}
$$

The real and the imaginary parts of Eq. (1.38) allow us to express the real, p_1, and the imaginary, p_2, components of the canonical momentum via the real and the imaginary parts of the return time (for above threshold harmonics):

$$
p_1 = \cosh(\phi_r'')\sin(\phi_r') + \gamma_N, \tag{1.45}
$$

$$
p_2 = \sinh(\phi_r'')\cos(\phi_r'). \tag{1.46}
$$

The real and the imaginary parts of Eq. (1.36),

$$
p_1 = \cosh(\phi_i'')\sin(\phi_i'), \tag{1.47}
$$

$$
p_2 + \gamma = \sinh(\phi_i'')\cos(\phi_i'), \tag{1.48}
$$

allow us to express the real, ϕ_i', and the imaginary, ϕ_i'', ionization times via p_1 and
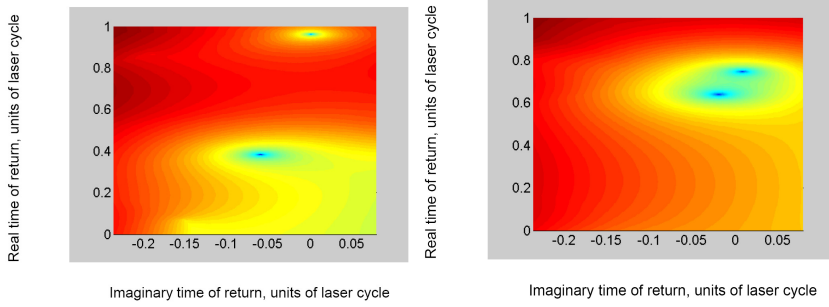
Figure 1.3 Surface in Eq. (1.41) for $I_p = 15.6$ eV, $I = 1.3 \cdot 10^{14}$ W/cm^2, $\hbar\omega = 1.5$ eV. Left panel: $N = 11$; two minima corresponding to short ($\phi_r' \sim 0.4$) and to long ($\phi_r' \sim 1$) trajectories, respectively. Right panel: $N = 27$; the two minima corresponding to short and to long trajectories are merging together.

p_2:

$$\phi_i' = \arcsin(\sqrt{(P-D)/2}), \tag{1.49}$$
$$\phi_i'' = \text{arcosh}(\sqrt{(P+D)/2}), \tag{1.50}$$

where

$$P = p_1^2 + \tilde{\gamma}^2 + 1,$$
$$D = \sqrt{P^2 - 4p_1^2},$$
$$\tilde{\gamma} = \gamma + p_2. \tag{1.51}$$

Now we can use our recipe:

- Pick a grid of values ϕ_r', ϕ_r'' in the complex plane of the return times ϕ_r;
- Pick a point ϕ_r', ϕ_r'' and calculate p_1, p_2 using Eqs. (1.45,1.46) and ϕ_i', ϕ_i'' using Eqs. (1.49,1.50);
- Substitute p_1, p_2, ϕ_i', ϕ_i'' into Eqs. (1.43,1.44);
- Plot the function $F \equiv F_1^2 + F_2^2$ in the plane of the real and the imaginary return times;
- Look for the minima, see Fig. 1.3.

Instead of reading out the solutions from the graph, one can find the minima using the gradient method. An alternative algorithm using the same ideas is described in Appendix D.

The imaginary and the real return times (Fig. 1.4, right panel) define the integration contour in the complex plane: only along this contour the energy of return and therefore the energy of the emitted photon are real. This energy is shown in Fig. 1.4 (left panel) vs the real component of the return time for typical experimental conditions.

The cut-off (maximal energy) corresponds to about $3.17\,U_p + 1.32\,I_p$, see Lewenstein *et al.* (1994). There are two different trajectories returning at different times that lead to the same re-collision energy. Those returning earlier correspond to shorter
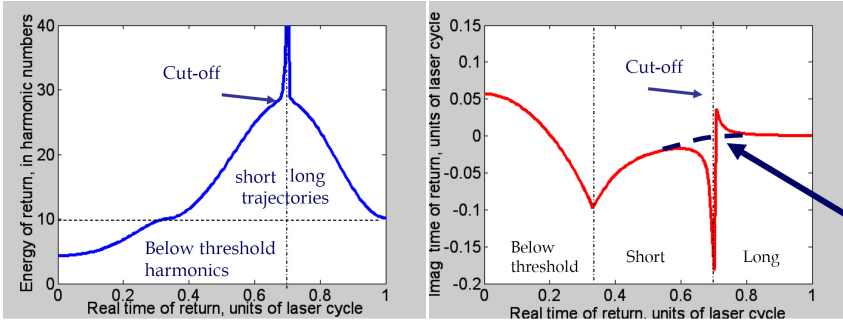
Figure 1.4 Left panel: Emission energy, $E(t_r) + I_p = N\omega$, vs real time of return for $I_p = 15.6$ eV, $I = 1.3 \cdot 10^{14}$ W/cm^2. Right panel: Imaginary time of return vs real time of return. The solution diverges in the cut-off region. The thick blue line schematically shows the desired outcome of the regularization procedure.

excursion and are called 'short trajectories', those returning later are called 'long trajectories' as they correspond to larger excursions and longer travel times.

Fortunately for attosecond imaging, the contributions of the long and the short trajectories to the harmonic emission separate in the macroscopic response: the harmonic light diverges differently for those trajectories, and thus the signals coming from short and long trajectories can be collected separately. As a result, each harmonic N can be associated with a particular time delay between ionization and recombination, $t'_r - t'_i$, and therefore each harmonic takes a snapshot of the recombining system at a particular moment of time. This time-energy mapping, see (Lein (2005), Baker *et al.* (2006), Shafir *et al.* (2012)), is the basis for attosecond time resolution in high harmonic spectroscopy.

As mentioned in the previous section, the stationary phase (saddle point) method for the integral over return times t breaks down near the cut-off, where the two stationary points (short and long trajectories) begin to coalesce and the second derivative of the phase S with respect to the return time is equal to zero, $\partial^2 S/\partial t^2 = 0$. The regularization of the solutions in the cut-off region is discussed in Appendix C. Here, we shall proceed with the analysis of the stationary phase equations and turn to the ionization times.

The concept of ionization time together with the semiclassical (trajectory) perspective on ionization has been first introduced by V. Popov and co-workers (see Perelomov *et al.* (1966, 1967); Perelomov and Popov (1967); Popov *et al.* (1968)). Just like in the Lewenstein model described above, the concept of trajectories arises from the application of the saddle point method to the integral describing ionization [3]

---

3) Eq. (1.52) corresponds to the length-gauge SFA result for ionization. Eq. (1.52) also results from the PPT approach under the approximation, substituting the laser-dressed bound wave-function by the field-free ground state. Thus, the PPT approach allows one to identify the approximations in Eq. (1.52) for short-range potentials. The SFA is inaccurate, because the Vokov states are not sufficiently accurate even for short-range potentials.

$$a_{ion}(\mathbf{p}, t) = -i \int_0^T dt' \, e^{-iS(\mathbf{p}, T, t')} \, \Upsilon(\mathbf{p} + \mathbf{A}(t')). \tag{1.52}$$

Here the upper limit of the integral in the action $S(\mathbf{p}, T, t')$ Eq.(1.21) is the real time T, at which the liberated photoelectron is observed (detected), function $\Upsilon(\mathbf{p} + \mathbf{A}(t'))$ (see 1.23) contains the Fourier transform of the bound state wave-function. The saddle point method applied to Eq.(1.52) yields the ionization amplitude:

$$a_{ion}(\mathbf{p}, t) = \left[\frac{2\pi}{iS''_{t_i, t_i}} \right]^{1/2} e^{-iS(\mathbf{p}, T, t_i)} \, \Upsilon(\mathbf{p} + \mathbf{A}(t_i)), \tag{1.53}$$

where t_i is the complex saddle point given by the condition

$$\frac{[\mathbf{p} + \mathbf{A}(t_i)]^2}{2} + I_p = 0. \tag{1.54}$$

The saddle point method selects specific moments of time t_i when ionization occurs. At these times the instantaneous electron energy $\frac{[\mathbf{p} + \mathbf{A}(t_i)]^2}{2}$ is equal to the energy of the ground state and therefore the instantaneous momentum of the electron hits the pole of the bound state wave-function in the momentum space. In the vicinity of the pole, the wave-function in the momentum space is determined by the asymptotic part of the wave-function in the coordinate space. Thus, in contrast to one-photon ionization, which probes the bound wave function near the core, the strong field ionization probes the asymptotic part of the bound wave function:

$$\langle \mathbf{r} | g \rangle \simeq C_{\kappa l} \kappa^{3/2} \frac{e^{-\kappa r}}{\kappa r} Y_{lm}(\frac{\mathbf{r}}{r}). \tag{1.55}$$

Equation (1.55) restricts our analysis to short range potentials (see Torlina and Smirnova (2012) for consistent analytical treatment of strong-field ionization from a long range (Coulomb) potential, $\kappa = \sqrt{2I_p}$, $C_{\kappa l}$ is a constant, $Y_{lm}(\frac{\mathbf{r}}{r})$ reflects the angular structure of the bound state. For Coulomb potential $-Q/r$, the asymptotic expression (1.55) must be multiplied by $(\kappa r)^{Q/\kappa}$:

$$\langle \mathbf{r} | g \rangle \simeq C_{\kappa l} \kappa^{3/2} \frac{e^{-\kappa r}}{\kappa r} (\kappa r)^{Q/\kappa} Y_{lm}(\frac{\mathbf{r}}{r}). \tag{1.56}$$

Evaluating the Fourier transform of (1.55) we obtain explicit expression for $\Upsilon(\mathbf{p})$ (see Perelomov *et al.* (1966)):

$$\Upsilon(\mathbf{p}) = \left(\frac{2\kappa}{\pi} \right)^{1/2} C_{\kappa l} \, Y_{lm}(\frac{\mathbf{p}}{p}). \tag{1.57}$$

Evaluation of the spherical function $Y_{lm}(\frac{\mathbf{p}}{p})$ at the pole $p = \pm i\kappa$ yields (see Perelomov *et al.* (1966) and also Barth and Smirnova (2011, 2013) for circularly polarized fields) :

$$Y_{lm}(\frac{\mathbf{p}}{p})|_{p=\pm i\kappa} = C_{lm} \left(\frac{\pm p_\perp}{\kappa} \right)^m e^{im\phi_p}, \tag{1.58}$$

$$C_{lm} = \frac{1}{2^{|m|}|m|} \sqrt{\frac{(2l+1)(l+|m|)!}{4\pi(l-|m|)!}}, \tag{1.59}$$

where $p_\perp$ is the electron transverse momentum at the detector and ϕ_p is the azimuthal angle of the electron momentum at the detector. Taking into account that $S''_{t_i,t_i} = (\mathbf{p} + \mathbf{A}(t_i))\mathbf{A}'(t_i)$ can be written as

$$iS''_{t_i,t_i} = \mu\kappa F(t_i), \tag{1.60}$$

$$\mu = -\text{sign}(F(t_i)), \tag{1.61}$$

we obtain the final expression for the amplitude of single ionization burst at complex time $t_i(\mathbf{p})$, specified by the final momentum of the electron $\mathbf{p}$:

$$a_{ion}(\mathbf{p}) = 2C\sqrt{\frac{1}{\mu F(t_i)}}\left(\mu\frac{p_\perp}{\kappa}\right)^m e^{-iS(\mathbf{p},T,t_i(\mathbf{p}))}\,e^{im\phi_p}, \tag{1.62}$$

$$C = C_{lm}C_{\kappa l}. \tag{1.63}$$

Note that both the real and the imaginary component of $t_i(\mathbf{p})$ depend on laser parameters. Therefore, the dependence of the pre-exponential factor (prefactor) in $a_{ion}(\mathbf{p})$ on the laser field is not simply $F^{-1/2}$ as illustrated below for the ionization at the maximum of the laser cycle. Indeed, the sub-cycle dynamics in the prefactor is much slower than in the exponent, thus one can also use a simpler expression for S''_{t_i,t_i} corresponding to its value at the maximum of the laser field (Perelomov *et al.* (1966)):

$$iS''_{t_i,t_i} = -\frac{\kappa^2}{\omega}\frac{\sqrt{1+\gamma^2}}{\gamma}. \tag{1.64}$$

Omitting the sub-cycle dynamics in the prefactor we obtain a simpler expression for the amplitude of single ionization burst at the time $t_i(\mathbf{p})$, consistent with the one derived by Perelomov *et al.* (1966):

$$a_{ion}(\mathbf{p}) = 2C\left[\frac{-\gamma\omega}{\kappa\sqrt{1+\gamma^2}}\right]^{1/2}\left(\frac{\mu p_\perp}{\kappa}\right)^m e^{-iS(\mathbf{p},T,t_i(\mathbf{p}))+im\phi_p}. \tag{1.65}$$

At the same level of approximation, i.e. neglecting the sub-cycle dynamics in the prefactor, the effects of the Coulomb potential are incorporated by simply adding the factor $\left(\frac{2\kappa^3}{F}\right)^{Q/\kappa}$:

$$a_{ion}(\mathbf{p}) = 2C\left(\frac{2\kappa^3}{F}\right)^{\frac{Q}{\kappa}}\left[\frac{-\gamma\omega}{\kappa\sqrt{1+\gamma^2}}\right]^{\frac{1}{2}}\left(\frac{\mu p_\perp}{\kappa}\right)^m e^{-iS(\mathbf{p},T,t_i(\mathbf{p}))+im\phi_p}. \tag{1.66}$$

The sub-cycle Coulomb effects are derived in Torlina and Smirnova (2012). Note that in the rigorous analysis within the analytical R-matrix (ARM) approach, which consistently treats the Coulomb effects both in bound and continuum states (Torlina and Smirnova (2012); Kaushal and Smirnova (2013)), the pole in $\Upsilon(\mathbf{p} + \mathbf{A}(t_i))$ does not appear, because the radial integration is removed due to the use of the Bloch operator (Bloch (1957)). Therefore, it removes all technical aspects and additional terms associated with the presence and the strength of the pole.

Note that the expression for the induced dipole, Eq. (1.42), contains terms that look very much like the ionization amplitude Eq. (1.53). This observation is important,
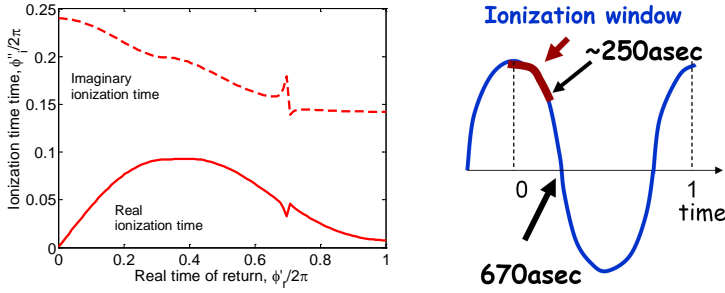
Figure 1.5 Left panel: Real and imaginary ionization times vs real return time for
$I_p = 15.6$ eV, $I = 1.3 \cdot 10^{14}$ W/cm^2, $\hbar\omega = 1.5$ eV. Right panel: Cartoon illustrating the
ionization window. Ionization occurs around the field maximum within an approximately
250 as time window (corresponding to the maximum value of the real ionization time).

as it suggests the connection of the harmonic response to ionization, as in the simple
man model. However, the story is more subtle: the stationary momenta $\mathbf{p}_s$ in the
harmonic dipole are complex-valued, while here they are real observable quantities.

The integral Eq.(1.52) has been extensively studied by Keldysh, Popov, Perelomov,
Terent'ev, and many others. The semiclassical picture in Perelomov *et al.* (1966,
1967); Perelomov and Popov (1967); Popov *et al.* (1968), enabled by the applica-
tion of saddle point method, shows that strong-field ionization can be understood as
tunnelling through the oscillating barrier created by the laser field. The tunneling
picture clarifies the sensitivity of strong field ionization to the asymptotic 'tail' of the
bound wave-function (see Eq.(1.55,1.56)), since it is this asymptotic part that 'leaks'
through the barrier. The modulus of the ionization amplitude is associated with the
imaginary part of the action S in Eq. (1.53, 1.62, 1.65, 1.66). This imaginary part
is only accumulated from t_i to t_i', since in the photoionization problem the canon-
ical momentum registered at the detector is real and the integration over time also
proceeds along the real time axis between t_i' and the observation time t.

This is why the complex saddle point t_i is associated with the time at which the
electron enters the classically forbidden region – the tunnelling barrier – while the real
part of the complex saddle point t_i', after which changes to the ionization amplitude
stop[4], is associated with the time of exit from the classically forbidden 'under-the-
barrier' region. The same reasoning can be extended to the ionization times arising
within the semiclassical picture of harmonic generation, see Fig. (1.5). However,
the ionization times in high harmonic generation are somewhat different due to the
fact that $\mathbf{p}_s$ are complex-valued. In the next section we will consider the connection
between these two times.

The imaginary ionization time defines the ionization probability. Since the imagi-

4) Rigorously, this statement is only true for short range potentials. Long-range electron-core interactions
lead to additional modifications of the ionization amplitude after t_i' (Torlina and Smirnova (2012), Tor-
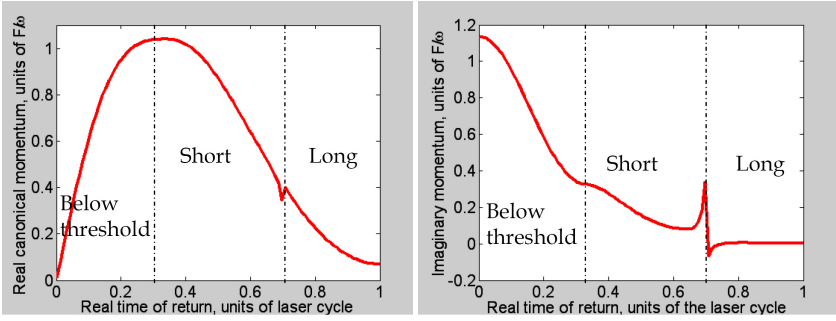lina *et al.* (2013)).

Figure 1.6 Left panel: Real canonical momentum vs real return time for $I_p = 15.6$ eV, $I = 1.3 \cdot 10^{14}$ W/cm^2, $\hbar\omega = 1.5$ eV. Right panel: Imaginary canonical momentum vs real return time.

nary component of the ionization time is larger for short trajectories, these trajectories have a lower chance of being launched compared to the long ones. The range over which the real part of the ionization time changes within the quarter-cycle defines the duration of the 'ionization window'. Typically, for a $\lambda \simeq 800$ nm driving laser field and a laser intensity of $I \sim 10^{14}$ W/cm^2, the ionization times (their real part) are spread within ∼250 attoseconds around the instantaneous maximum of the laser field (see Fig. 1.5). Thus, strong-field ionization is an intrinsic attosecond process. Note that the quantum 'ionization window' is shorter than the classical one (see Fig. 1.1), as according to the classical simple man picture ionization happens at any phase of the laser field.

Figure 1.6 shows the saddle point solutions for the electron canonical momentum.

In photoionization, the electron canonical momentum is always real, since it is the observable registered at the detector. In contrast, in harmonic generation the observable registered at the detector is the emitted photon, and hence it is the photon energy that must be real. As a result, the electron canonical momenta in HHG are complex. Electrons on long trajectories have a very small imaginary canonical momentum. Therefore, it is a very good approximation to associate long trajectories with photoelectrons. Note that the maximum of the real canonical momentum is about $p_{\max} \simeq A_0$. In the photoelectron perspective $p_{\max}$ corresponds to an energy of $2U_p$ at the detector - the cut-off energy for the so-called direct photoelectrons, i.e. those that have not substantially changed their momentum after ionization.

The imaginary part of the canonical momentum can be quite large for short trajectories. The complex-valued solutions, not only for the ionization times, but also for the recombination times and the electron canonical momenta, challenge our understanding of the underlying physical picture of harmonic generation. If the first step of high harmonic generation is ionization, then why do these liberated electrons have complex canonical momenta? Does this mean that these electrons have not been ionized? Can we factorize the harmonic dipole into ionization, propagation and recombination? The next section explores this opportunity.

20

1.6
Factorization of the HHG dipole: simple man on a complex plane

Having derived the analytical expressions for the HHG dipole, can we identify the simple man model in it, within the consistent quantum approach? To do this, we need to factorize the harmonic dipole into the three steps: ionization, propagation and recombination. That is, we have to re-write the dipole as a product of the ionization amplitude, the propagation amplitude and the recombination amplitude.

Such factorization of the harmonic dipole is not just curiosity driven. It is important for extending the modelling of harmonic emission to complex systems. Once the three steps are identified, the respective amplitudes can be imported from different approaches, tailored to calculate specifically ionization or recombination in complex systems.

The factorization of the harmonic dipole runs into two types of problems: technical and conceptual. The technical problems arise from the fact that the original three-step (simple man) model is formulated in the time domain. The three processes – ionization, propagation and recombination – are the sequence of subsequent time-correlated events. The harmonic spectrum formally corresponds to the harmonic dipole in the frequency domain, where the three processes become entangled: recall the contribution of different quantum trajectories to the same photon energy. Thus, rigorous factorization in the frequency domain is only possible in the cut-off region, where short and long solutions merge, see Frolov *et al.* (2009) [5].

The conceptual problem is due to the complex canonical momentum of the electron responsible for HHG. Ionization in terms of creating photoelectrons with real canonical momenta does not appear to fit into the HHG picture. Can we build an alternative model of HHG based entirely on photoelectrons, i.e. those electrons which are indeed ionized at the first step?

Let us address these issues step by step, starting with the factorization of the harmonic dipole in the frequency domain (Frolov *et al.* (2009); Kuchiev and Ostrovsky (1999); Morishita *et al.* (2008)) and the time domain (Ivanov *et al.* (1996)). The former involves the factorization of Eq. (1.25), the latter factorizes Eq. (1.24).

1.6.1
Factorization of the HHG dipole in the frequency domain

To re-write the harmonic dipole in the semi-factorized form, we can take Eq. (1.42) and split the action integral S that enters the phase of this expression into the following three time intervals: from t_i to t_i', from t_i' to t_r', and from t_r' to t_r (see Fig. 1.2). Then we can identify the group of terms that looks like the ionization amplitude sim-

---

5) Note that the quantitative rescattering theory (see Le *et al.* (2009)) postulates that one can factor out the recombination step in the frequency domain harmonic dipole. This postulate is supported by the results of numerical simulations demonstrating approximate factorization in the cut-off region, see Morishita *et al.* (2008).

ilar to that given by Eq. (1.53),

$$a_{ion}(\mathbf{p}_s, t_i) = \left[\frac{2\pi}{iS''_{t_i,t_i}}\right]^{1/2} e^{-iS(\mathbf{p}_s,t'_i,t_i)} \Upsilon(\mathbf{p}_s + \mathbf{A}(t_i)). \tag{1.67}$$

The ionization amplitude is associated with the first time interval, from t_i to t'_i, and only the part of the action integral from t_i to the real time axis $t'_i = \text{Re}(t_i)$ enters this amplitude. For a short-range potential (neglecting the sub-cycle effects in the prefactor):

$$a_{ion}(\mathbf{p}_s) = 2C \sqrt{\frac{-\tilde{\gamma}\omega}{\kappa\sqrt{1+\tilde{\gamma}^2}}} \left(\frac{p_{s\perp}}{\kappa}\right)^m e^{-iS(\mathbf{p}_s,T,t_i)+im\phi_{p_s}}. \tag{1.68}$$

Constant C is specified in Eq. (1.63). The momentum $\mathbf{p}_s$ is given by the full set of saddle point conditions for t_i, t_r, and $\mathbf{p}_s$:

$$\frac{[\mathbf{p}_s + \mathbf{A}(t_i)]^2}{2} + I_p = 0,$$

$$\int_{t_i}^{t_r} [\mathbf{p}_s + \mathbf{A}(t')]dt' = 0,$$

$$\frac{[\mathbf{p}_s + \mathbf{A}(t_r)]^2}{2} + I_p = N\omega. \tag{1.69}$$

Note that t_i in HHG and and t_i in ionization are different, that is why in Eq. 1.65 we use γ and $\mathbf{p}$, whereas in Eq. (1.70) we use $\tilde{\gamma}$ (see Eq.1.51) and $\mathbf{p}_s$. If imaginary part of $\mathbf{p}_s$ is equal to zero, then $\tilde{\gamma} = \gamma$. For Coulomb potential (neglecting the sub-cycle effects in the prefactor):

$$a_{ion}(\mathbf{p}_s) = 2C \left(\frac{2\kappa^3}{F}\right)^{\frac{Q}{\kappa}} \sqrt{\frac{-\tilde{\gamma}\omega}{\kappa\sqrt{1+\tilde{\gamma}^2}}} \left(\frac{p_{s\perp}}{\kappa}\right)^m e^{-iS(\mathbf{p}_s,T,t_i)+im\phi_{p_s}}. \tag{1.70}$$

Now consider the next time interval, from t'_i to t'_r. The prefactor arising from saddle point integration over the electron momenta $\mathbf{p}$ leads to the term

$$\frac{(2\pi)^{3/2}}{\sqrt{\det(iS''_{\mathbf{p}_s,\mathbf{p}_s})}} = \frac{(2\pi)^{3/2}}{(i(t_r - t_i))^{3/2}}. \tag{1.71}$$

This term describes the free spreading of the electron wavepacket between t_i and t_r. Thus, we associate the following group of terms with the propagation amplitude:

$$a_{prop}(\mathbf{p}_s, t_r, t_i) = \frac{(2\pi)^{3/2}}{(i(t_r - t_i))^{3/2}} e^{-iS(\mathbf{p}_s,t'_r,t'_i)}. \tag{1.72}$$

Note that the denominator includes the complex-valued times t_i and t_r.

Finally, the recombination amplitude is represented by the recombination matrix element $\mathbf{d}^*(\mathbf{p}_s + \mathbf{A}(t_r))$ and can be associated with the following group of terms:

$$\mathbf{a}_{rec}(\mathbf{p}_s, t_i) = \left[\frac{2\pi}{iS''_{t_r,t_r}}\right]^{1/2} e^{-iS(\mathbf{p}_s,t_r,t'_r)+iN\omega t_r} \mathbf{d}^*(\mathbf{p}_s + \mathbf{A}(t_r)), \tag{1.73}$$

where $S''_{t_r, t_r} = -\sqrt{2(N\omega - I_p)}F(t_r)$ for a linearly polarized field. As a result, the total dipole is formally written as

$$\mathbf{D}(N\omega) = \sum_{j=1}^{4M} \mathbf{a}_{rec}(\mathbf{p}_s, t_r^{(j)}) a_{prop}(\mathbf{p}_s, t_r^{(j)}, t_i^{(j)}) a_{ion}(\mathbf{p}_s, t_i^{(j)}), \qquad (1.74)$$

where the index j labels the saddle points. However, in contrast to photoelectrons, the electrons involved in HHG have complex canonical momenta $\mathbf{p}_s$. Therefore, the imaginary part of the action is accumulated not only 'under the barrier', from t_i to t_i', but also all the way between t_i' and t_r. Thus, factoring out ionization as the first step of HHG is not that convincing. Similarly, the recombination step involves not only the recombination dipole, but also the possible change in the amplitude due to the imaginary contribution to the action between t_r' and t_r. Thus, while we can formally associate several groups of terms in the harmonic dipole (1.74) with amplitudes of ionization, propagation, and recombination, the complex-valued electron momenta make such identification somewhat stretched.

An additional point to note is that the three amplitudes are also entangled due to the sum over the different saddle points in Eq. (1.74). Even if we only consider contributions of the two most important trajectories, short and long, the sum entangles their contributions and also mixes up the contributions from different half-cycles. Importantly, a finite pulse duration leads to a different mapping between the given harmonic number and the ionization-recombination times for each half-cycle.

A practical approach to factorization realized in the so-called quantitative rescattering theory (Le *et al.* (2009)) is to assume that $\mathbf{a}_{rec}(\mathbf{p}_s(N), t_r^{(j)}(N)) = \mathbf{a}_{rec}(N\omega)$ for all j yielding:

$$\mathbf{D}(N\omega) = \mathbf{a}_{rec}(N\omega) \sum_{j=1}^{4M} a_{prop}(\mathbf{p}_s, t_r^{(j)}, t_i^{(j)}) a_{ion}(\mathbf{p}_s, t_i^{(j)}), \qquad (1.75)$$

This approximation breaks down in the following cases:

1) In two-color orthogonally polarized fields Morales *et al.* (2012). In this case more than two trajectories returning at different angles can map into the same return energy Morales *et al.* (2012). Such trajectories must correspond to different recombination dipoles for different angles, violating 1.75.
2) In the vicinity of the structural minimum of the recombination matrix element, or when the phase of the matrix element changes rapidly (Smirnova *et al.* (2009b), Patchkovskii *et al.* (2012)).
3) When the sub-cycle dynamics associated with the electron interaction with the core potential can not be neglected.

These technical problems can be remedied by looking at the dipole in the time domain.

1.6.2
Factorization of the HHG dipole in the time domain

There are several advantages of using the time-domain dipole. For starters, if we do not perform the Fourier transform analytically, the time t_r no longer has to be complex. With the Fourier integral performed using a standard FFT routine, we can keep t_r on the real time axis. The number of saddle-point conditions is also conveniently reduced to two (one of them, for the momentum $\mathbf{p}_s$, is in general 3-dimensional)

$$\frac{[\mathbf{p}_s + \mathbf{A}(t_i)]^2}{2} + I_p = 0,$$

$$\int_{t_i}^{t_r} [\mathbf{p}_s + \mathbf{A}(t')]\, dt' = 0, \tag{1.76}$$

with t_r being the parameter, instead of the harmonic number N.

In the time domain, it is natural to sort the contributions to the induced dipole according to the corresponding ionization bursts. Then, for each half-cycle j, there is a single ionization burst j at time $t_i^{(j)}$ that contributes to the induced dipole as a function of the real return time t_r, see left panel of Fig. 1.5. After saddle-point integration, this contribution is:

$$\mathbf{D}^{(j)}(t_r) = i\left[\frac{2\pi}{iS''_{t_i^{(j)},t_i^{(j)}}}\right]^{1/2} \frac{(2\pi)^{3/2}}{\sqrt{\det(iS''_{\mathbf{p}_s,\mathbf{p}_s})}} \times$$

$$\times\, \mathbf{d}^*(\mathbf{p}_s + \mathbf{A}(t_r))\, e^{-iS(\mathbf{p},t_r,t_i^{(j)})}\, \Upsilon(\mathbf{p}_s + \mathbf{A}(t_i^{(j)})),$$

$$S(\mathbf{p}_s, t_r, t_i) \equiv \frac{1}{2}\int_{t_i}^{t_r}[\mathbf{p}_s + \mathbf{A}(\tau)]^2 d\tau + I_p(t_r - t_i), \tag{1.77}$$

with $\det(iS''_{\mathbf{p}_s,\mathbf{p}_s}) = \left[i(t_r - t_i^{(j)})\right]^{3/2}$ (see also Eq. 1.71). Just as in the frequency domain, up to a global phase factor the dipole can be written as a product of three amplitudes:

$$\mathbf{D}^{(j)}(t_r) = \mathbf{a}_{rec}(\mathbf{p}_s, t_r)a_{prop}(\mathbf{p}_s, t_r, t_i^{(j)})a_{ion}(\mathbf{p}_s, t_i^{(j)}). \tag{1.78}$$

The ionization and the propagation amplitudes entering this expression are given by Eqs. (1.67,1.72). The recombination amplitude is simply equal to the recombination matrix element $\mathbf{d}^*(\mathbf{p}_s + \mathbf{A}(t_r))$, as we have not performed the Fourier transform yet. Equation (1.78) is the natural mathematical formulation of the three step model, which is intrinsically sub-cycle.

If we ignore multiple returns and very long trajectories, then for each t_r there is only one ionization burst to deal with. As opposed to the frequency domain, the contributions of the long and the short trajectories from this ionization burst are not yet mixed – they are separated in time. This is very convenient if you need to look at the contribution of only the short, or only the long trajectories: it is straightforward to

24

add a time-domain filter that would filter out the unwanted contributions. Essentially, this would correspond to making a window Fourier transform of the time-domain harmonic dipole. The inclusion of the contribution of multiple returns is rarely required for typical experimental conditions.

To model the full $\mathbf{D}(t_r)$ one needs to model ionization, recombination and propagation separately for each half-cycle, and then collect the contributions from each half-cycle (each ionization burst):

$$\mathbf{D}(t_r) = \sum_j \mathbf{D}^{(j)}(t_r). \tag{1.79}$$

To obtain the harmonic spectrum, we have to perform the Fourier transform, which is convenient to do numerically using a FFT routine. There are two possible approaches to implement the Fourier transform.

Integration along Lewenstein's contour. In this approach, the Fourier transform is performed along the time contour in the complex plane $t_r = t_r' + it_r''$. In this case the argument of the recombination dipole $\mathbf{p}_s + \mathbf{A}(t_r)$ remains real and so does the recollision energy $E_{rec}(t_r)$. Since it is difficult to *numerically* perform an integration along a complex contour

$$\mathbf{D}(N\omega) = \int dt_r \, e^{-N\omega t_r''} \, \mathbf{D}(t_r) \, e^{iN\omega t_r'}, \tag{1.80}$$

one can use variable substitution and integrate over the real return times t_r':

$$\mathbf{D}(N\omega) = \int dt_r' \left[\frac{dt_r}{dt_r'} e^{-[E_{rec}(t_r)+I_p]t_r''} \right] \mathbf{D}(t_r') \, e^{iN\omega t_r'}, \tag{1.81}$$

$$N\omega = E_{rec}(t_r) + I_p, \tag{1.82}$$

$$E_{rec}(t_r) = [\mathbf{p}_s + \mathbf{A}(t_r)]^2/2. \tag{1.83}$$

The derivative in the square bracket is associated with the variable substitution.

Note that Eq. (1.81) contains one approximation: the term $e^{-(N\omega)t_r''}$ is modified according to the energy conservation $N\omega = E_{rec}(t_r) + I_p$. However, the integration of Eq. (1.81) is not very convenient due to the additional effort associated with the need to avoid the divergence of $\frac{dt_r}{dt_r'}$ in the cut-off region (see Fig. 1.4).

HHG dipole on the real time axis. To keep things simple, one can keep the half-cycle harmonic dipole on the real time axis:

$$\mathbf{D}^{(j)}(t) = \mathbf{a}_{rec}(\mathbf{p}_s, t) a_{prop}(\mathbf{p}_s, t, t_i^{(j)}) a_{ion}(\mathbf{p}_s, t_i^{(j)}), \tag{1.84}$$

where the saddle points $\mathbf{p}_s$ and $t_i^{(j)}$ are given by the Eqs. (1.76) and the index j labels different solutions corresponding to the same return time t.

In this 'real-time-axis' approach, the return time t is a parameter: we have to find t_i and $\mathbf{p}_s$ for each t. This can be done using a procedure similar to that described in the previous section, only simpler. Specifically, we introduce the dimensionless variables $\phi = \omega t$ and $p/(F/\omega) = p_1 + ip_2$. For a linearly polarized field $p_{s,\perp} = 0$. For each real ϕ we use the Eqs. (1.43,1.44) with $\phi_r'' = 0$ and $\phi_r' \equiv \phi$:

$$F_1(\phi) = p_1(\phi - \phi_i') + p_2\phi_i'' - \cos(\phi_i')\cosh(\phi_i'') + \cos(\phi) = 0, \tag{1.85}$$

$$F_2(\phi) = -p_1\phi_i'' + p_2(\phi - \phi_i') + \sin(\phi_i')\sinh(\phi_i'') = 0. \tag{1.86}$$

We can now use the Eqs. (1.47,1.48) to express p_1 and p_2 in terms of ϕ_i' and ϕ_i''. Then, we build the surface $F(\phi) = F_1^2 + F_2^2$ for each ϕ. Next, we find the minima on this surface. Alternatively, we can use p_1 and p_2 as our variables, expressing ϕ_i' and ϕ_i'' via p_1, p_2, then the minima on the surface $F_1^2 + F_2^2$ will yield the real, p_1, and the imaginary, p_2, components of the canonical momentum, and then the Eqs. (1.49,1.50) yield the corresponding ionization times.

In this approach the divergence at the cut-off is avoided, since the divergence occurs in the complex plane of the return times when calculating the Fourier transform analytically using the saddle point method. The price to pay is that the recombination dipole has to be taken at the complex arguments $\mathbf{p}_s + \mathbf{A}(t)$ and the re-collision energy $E_{rec}(t)$ has an imaginary part. In practice, one can use the real part of the re-collision energy as the argument of the recombination dipole. If one wants to avoid this approximation, one has to extend the recombination dipoles into the complex plane of the electron momenta.

Thus, one can formally factorize the harmonic dipole in the time domain, overcoming the technical problems associated with the factorization. However, one has to keep in mind that the ionization amplitude has to be modified to include complex canonical momenta and slightly different ionizaton times. Fortunately, it does not lead to changes in angular factors, because $\Upsilon_n(\mathbf{p}_s + \mathbf{A}(t_i))$ remains the same. Indeed, both $\mathbf{p}_s$ and t_i are different in case of HHG and ionization, but the term $\mathbf{p}_s + \mathbf{A}(t_i) = i\mu\kappa$ (see Eq. 1.61) is the same in both cases. The changes appear in the phase $S(\mathbf{p}_s, t_r, t_i)$ and the sub-cycle core effects, i.e. everywhere where p_s and t_i contribute separately.

The conceptual problem associated with understanding the physical meaning of the complex electron momenta, especially in the context of the "ionization step", still remains. The next section shows how, and to what extent, this problem can be circumvented. It introduces the photoelectron model of HHG, where the electron canonical momentum is restricted to the real axis.

1.7
The photoelectron model of HHG: the improved simple man

In the standard simple man model, the electron motion between ionization and recombination is modelled using classical trajectories. Naturally, the electron velocity, the ionization time, and the recombination time are all real-valued quantities. In the quantum description, the rigorous approach based on the saddle point method leads to trajectories with complex-valued momenta and complex-valued ionization and recombination times. The presence of complex canonical momenta makes it difficult to identify the ionization step.

The complex-valued canonical momenta and recombination times arise from the requirement that the electron returns exactly to its original position. Since the tunnelling electron accumulates an imaginary displacement during its motion in the classically forbidden region, the complex-valued momenta and return times must compensate for this displacement.
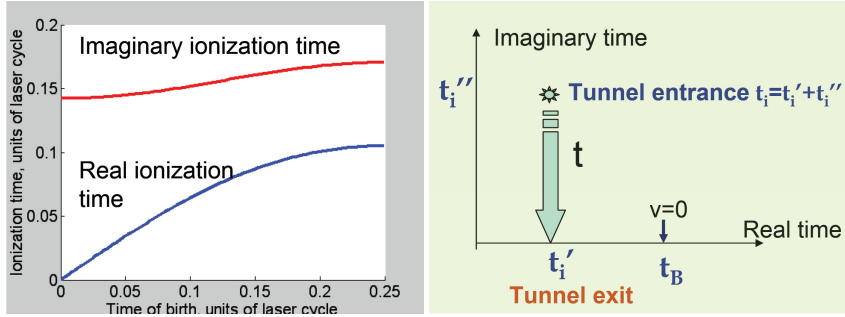
Figure 1.7 Left panel: Complex ionization time for photoelectrons $t_{i,ph}$ vs time of birth for $I_p = 15.6$ eV, $I = 1.3 \cdot 10^{14}$ W/cm^2, $\hbar\omega = 1.5$ eV. Right panel: Cartoon illustrating the connection between $t_{i,ph}$ and t_B: the electron exits the barrier with a negative velocity $\mathbf{v}(t_{i,ph}) = \mathbf{k}(t_{i,ph})$ (directed towards the core). Its velocity gradually decreases and becomes zero at the classical ionization time ($\mathbf{v}(t_B) = \mathbf{k}(t_B) = 0$) - the time of birth t_B.

This section shows that if we relax the return condition and neglect the imaginary displacement between t_i and $\mathrm{Re}(t_i)$, we can obtain the same re-collision energy for real-valued canonical momenta and for real-valued return times. We shall call this approach the photoelectron model since it allows one to incorporate standard strong-field ionization concepts in a natural manner. The ionization amplitude would then correspond to creating an electron with a real-valued canonical momentum, and the imaginary part of the action integral would only be accumulated between t_i and $\mathrm{Re}(t_i)$.

In the classical model, one assumes that the electron trajectory is launched at the real 'time of birth' t_B with zero instantaneous velocity. The electron instantaneous momentum at t_B can be written as $\mathbf{k}(t_B) = \mathbf{p} + \mathbf{A}(t_B) = \mathbf{0}$, where the canonical momentum $\mathbf{p}$ is a constant of motion (neglecting the core potential). The link between t_B and $\mathbf{p}$, $\mathbf{p} = -\mathbf{A}(t_B)$, links t_B via $[\mathbf{p} + \mathbf{A}(t_i)]^2 = -2I_p$ to the complex-valued ionization time t_i. In particular, for a linearly polarized laser field we have $[A(t_{i,ph}) - A(t_B)]^2 = -2I_p$. Note that this $t_{i,ph}$ is in general different from the ionization time t_i introduced in the previous section, since now the electron canonical momentum is forced to be real. The notation $t_{i,ph}$ stresses that this ionization time corresponds to photoelectrons, i.e. to electrons with real canonical momenta. Figure 1.7 shows the mapping between the time of birth and the complex time $t_{i,ph}$.

The photoelectron exits the tunnelling barrier at the real time, $\mathrm{Re}(t_{i,ph})$, and since $\mathrm{Re}(t_{i,ph})$ turns out to be smaller than t_B, the electron velocity at $\mathrm{Re}(t_{i,ph})$ is directed towards the core. It gradually decreases until becoming equal to zero at t_B. The difference between $\mathrm{Re}(t_{i,ph})$ and t_B is small near the peak of the oscillating electric field, but increases as the field approaches zero. While the times t_B are always spread within one quarter-cycle, as in the classical model, the times $\mathrm{Re}(t_{i,ph})$ are limited to a shorter fraction of the quarter-cycle, see Fig. 1.7.

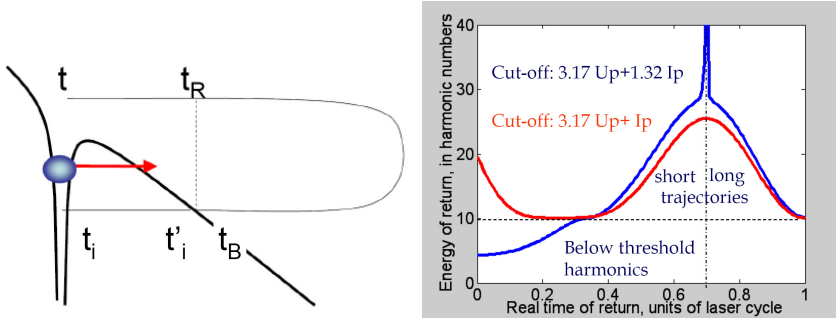We now turn to the classical return time t_R. In the original classical model, it is

Figure 1.8 Left panel: Physical picture of high harmonic generation in coordinate space and the meaning of different times. The electron enters the barrier at a complex time t_i and exits the barrier at the real time $t'_i = \mathrm{Re}\,t_i$. Its velocity goes through zero at a (later) time t_B. At the moment t_R the electron returns to the position it had at t_B, and at the moment t it returns to the origin. Right panel: The blue curve shows the electron return energy at the moment t in the Lewenstein model, while the red curve shows the electron return energy in the classical three-step model.

defined by the condition

$$\int_{t_B}^{t_R} [p + A(\tau)]\, d\tau = \int_{t_B}^{t_R} [-A(t_B) + A(\tau)]\, d\tau = 0. \tag{1.87}$$

However, since the electron is already offset from the origin at t_B,

$$\Delta z = \int_{t_{i,ph}}^{t_B} [A(\tau) - A(t_B)]\, d\tau, \tag{1.88}$$

it does not return to the origin at t_R, see Fig. 1.8.

The energy $E(t_R) = [A(t_R) - A(t_B)]^2/2$ in the classical model is shown in the right panel of Fig. 1.8, with the cut-off at $3.17\, U_p + I_p$. This cut-off is lower than in the quantum treatment, precisely because the electron has not yet returned to the core. The extra $0.32\, I_p$ in the quantum cut-off law, $3.17\, U_p + 1.32\, I_p$, is due to the extra energy accumulated by the electron while covering the extra distance Δz [6].

Can we improve these results if we allow the photoelectrons to travel a bit longer and allow them to return to the core? Why do not we continue to monitor the electron trajectory at times $t > t_R$ and register their energy at the time of return to the origin $t_{r,ph}$, ignoring whatever imaginary displacement they might have? There is just one problem with this plan: not all trajectories return to the core since we have limited the canonical momentum $p_{ph} = -A(t_B)$ to be no more than A_0. With this in mind, we shall take the energy at the closest approach to the origin as the return energy. We shall call this an improved three-step model or **the photoelectron model**.

---

[6] Interestingly, if one defines the experimental cut-off using the classical model, then the classical time-energy mapping is very similar to the quantum: t_R is very close to the real part of t_r. Since in the experiment the intensity is rarely known exactly, it is very difficult to differentiate between the classical (red) and the quantum (blue) return energies in Fig. 1.8.
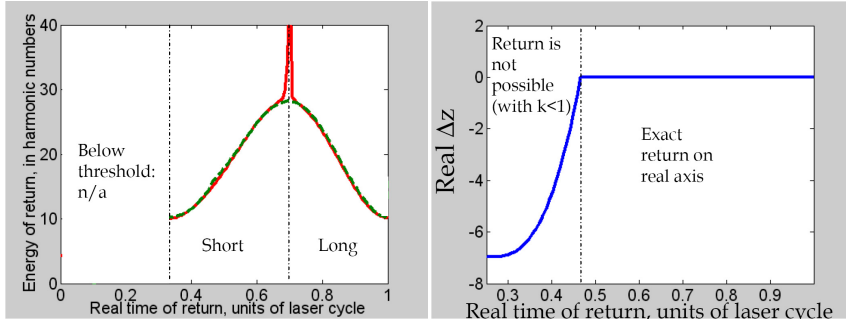
Figure 1.9 Left panel: Energy of return for the Lewenstein model (red) and for the photoelectron model (green) vs real return time for $I_p = 15.6$ eV, $I = 1.3 \cdot 10^{14}$ W/cm^2, $\hbar\omega = 1.5$ eV. Right panel: Real part of the electron displacement in the photoelectron model.

The model implies the neglect of the imaginary displacement and the minimisation of the real displacement between $t_{i,ph}$ and $t_{r,ph}$. The imaginary displacement has to be neglected since we do not have imaginary canonical momenta and imaginary return times to cover for it.

The photon energy resulting from the photoelectron model is $E_{rec}^{ph}(t)+I_p = \frac{dS}{dt_{r,ph}}$, where $S(p_{ph}, t_{r,ph}, t_{i,ph})$ is given by Eq. (1.21). It is in excellent agreement with the quantum photon energy (see Fig. 1.9, left panel) for all those trajectories for which the real part of the electron displacement from the origin passes through zero. This is the case for the long trajectories and for most of the short trajectories, except for the shortest ones. These latter ones are 'born' at the end of the ionization window and contribute to the lowest harmonics, just above the ionization threshold.

For short trajectories, the electron is decelerated by the laser field while returning to the core. Therefore, it needs a sufficiently high drift momentum to reach the origin. Since we have limited the canonical momentum $p = -A(t_B)$ below A_0, the shortest trajectories cannot quite make it to the core. For them, the time $t_{r,ph}$ corresponds to the closest approach to the core. A non-zero real displacement yields a deviation of the approximate action $S(p_{ph}, t_{r,ph}, t_{i,ph})$ from the real part of the exact action defined in the previous section, see the right panel of Fig. 1.9.

The action in this model is reproduced very well, since it is the time integral from the photon energy. Once the electron return energy is well-reproduced, so is the action, even if the end points t_i', t_r' are shifted.

From the mathematical perspective, the photoelectron model implies that when we perform the integrals, we expand the action not at the exact saddle point, but in its vicinity. In particular, we shift the center of the expansion for the canonical momentum from the complex plane to the real axis. The error introduced in the integral by this procedure is minimized if the new expansion point lies within the saddle point region of the exact complex saddle point of the multi-dimensional integral. Thus, the difference $\Delta p = p_q - p_{ph}$ between the stationary point solution for quantum orbits p_q and the canonical momentum in the improved three-step model p_{ph} should be less
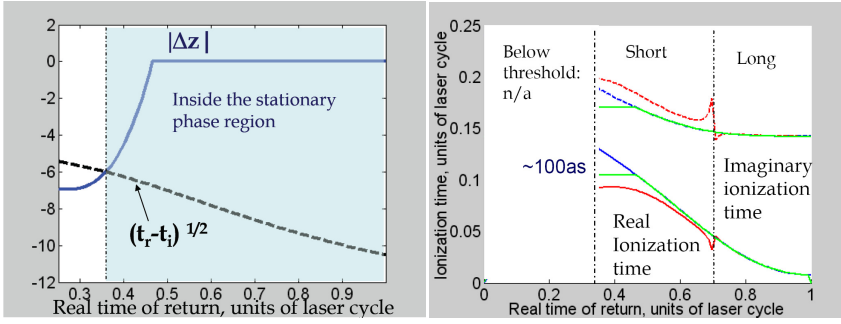
Figure 1.10 Left panel: Applicability region of the photoelectron model. The condition $|\Delta z| < (t_r - t_i)^{1/2}$ specifies the region of return times (filled) where the photoelectron model can be used. The calculation is shown for $I_p = 15.6$ eV, $I = 1.3 \cdot 10^{14}$ W/cm^2, $\hbar\omega = 1.5$ eV. Right panel: Real and imaginary ionization times for the Lewenstein model (red), the photoelectron model with canonical momentum less than A_0 (green), and for the canonical momentum not limited by this condition (blue).

than the size of the stationary point region: $|\Delta p| < |\partial^2 S/\partial p^2|^{-1/2} = (t_r - t_i)^{1/2}$. We can estimate $|\Delta p|$ as $|\Delta p| = |\Delta z/(t_r - t_i)|$, where $|\Delta z|$ includes the neglected imaginary displacement. This estimate yields $|\Delta z| < (t_r - t_i)^{1/2}$.

The left panel of Fig. 1.10 illustrates this condition for typical experimental parameters ($\omega = 0.057$ a.u., $I_p = 15.6$ eV, $I = 1.3 \cdot 10^{14}$ W/cm^2): the improved three step model cannot be applied for very short trajectories returning earlier than $\omega t_{r,ph} = 0.36$ or for harmonics lower than $N = 11$. Thus, for this particular set of parameters, all above threshold harmonics are within the applicability conditions of the improved three step model.

The right panel in Fig. 1.10 compares the ionization times resulting from the Lewenstein model and the photoelectron model of HHG. The ionization times coincide for the long trajectories. In this sense, the long trajectories indeed correspond to photoelectrons. The difference between the ionization times for the short trajectories is associated with the presence of imaginary canonical momenta in the Lewenstein model. For the shortest trajectories, the difference in the real ionization times is about 100 asec for the chosen laser parameters: the ionization window is wider for the photoelectron model. As for the imaginary component of the ionization times, they are smaller in the photoelectron model. Therefore, short trajectories are less suppressed in this model than in the full Lewenstein model.

Mathematically, implementing the photoelectron model requires only one approximation - relaxing the return condition. Note that the requirement of perfect return to the origin is an *artefact* of neglecting the size of the ground state in the saddle point analysis. If we take into account the size of the ground state, then the return condition will naturally be relaxed: to be able to recombine, the electron has to return to the core within the size of the ground state. From this perspective, the extension of the Lewenstein model to real systems, including molecules, should go hand in hand with relaxing the return condition for its real part.

Measurement of ionization times might allow one to differentiate between these two models and to pin down the nature of the electron trajectories responsible for HHG. In particular, the interesting question is wether the complex momenta are the artefac of the δ-like initial state, or are indeed relevant for realistic systems.

The accuracy of the first measurement Shafir $et\ al.$ (2012) was sufficient to distinguish between t_B and t_i', but not high enough to distinguish delays between t_i' (red curve, Fig. 1.10, left panel) and $t_{i,ph}'$ (green curve, Fig. 1.10 , left panel).

1.8
The multi-channel model of HHG: Tackling the multi-electron systems.

In multielectron systems, there are multiple ways of energy sharing between the liberated electron and the ion. The ion can be left in its ground or in one of its excited electronic states. These options are referred to as different ionization channels. Multiple ionization channels lead to multiple HHG channels: the returning electron can recombine with the ion in its ground or in one of its excited states.

Multiple HHG channels present different pathways connecting the same initial and final state - the ground state of the neutral system - via different intermediate electronic states of the ion. Thus, high harmonic emission in multielectron systems results from multichannel interference, see Smirnova $et\ al.$ (2009a), i.e. the interference of the harmonic light emitted in each channel. This interference naturally records multielectron dynamics excited upon ionization and probed by recombination, see Smirnova $et\ al.$ (2009a). How important are these multiple channels? How hard is it to excite the ion during strong-field ionization?

Strong-field ionization is exponentially sensitive to the ionization potential I_p, suggesting that after ionization the molecular ion is typically left in its ground electronic state. In the Hartree-Fock picture, this corresponds to electron removal from the highest occupied molecular orbital (HOMO). However, multiple ionization channels can be very important in molecules due to the geometry of the molecular orbitals and the proximity of the excited electronic states in the ion to the ground state.

The formalism described above, in the sections 1.1-1.7, is essentially a single-channel picture of HHG. It can be extended to multiple channels.

First, we introduce the Hamiltonian of an N-electron neutral molecule interacting with a laser field:

$$H^N = T_e^N + V_C^N + V_{ee}^N + V_L^N,$$

$$V_C^N = -\sum_m \sum_{i=1}^N \frac{Q_m}{|\mathbf{R}_m - \mathbf{r}_i|},$$

$$V_{ee}^N = \sum_{i \neq j}^N \frac{1}{|\mathbf{r}_i - \mathbf{r}_j|},$$

$$V_L^N = -\sum_i \mathbf{F}(t) \cdot \mathbf{d}_i = \sum_i \mathbf{F}(t) \cdot \mathbf{r}_i. \tag{1.89}$$

Here, the nuclei are frozen at their equilibrium positions $\mathbf{R}_m$, the index m enumerates the nuclei with charges Q_m, the superscript N indicates the number of electrons involved, T_e^N is the electron kinetic energy operator, V_C^N describes the Coulomb potential of the nuclei, V_{ee}^N describes the electron-electron interaction, and V_L^N describes the interaction with the laser field. Hats on top of operators are omitted.

We will also use the Hamiltonian of the ion in the laser field, $H^{(N-1)}$, and the Hamiltonian of an electron interacting with the laser field, the nuclei, and the $(N-1)$ electrons of the ion, $H^e = H^N - H^{(N-1)}$.

The Schrödinger equation for the N-electron wavefunction of the molecule, initially in its ground electronic state $\Psi_g^N(\mathbf{r})$, is

$$i\frac{\partial}{\partial t}\Psi^N(\mathbf{r}, t) = H^N\Psi^N(\mathbf{r}, t),$$
$$\Psi^N(\mathbf{r}, t = t_0) = \Psi_g^N(\mathbf{r}). \tag{1.90}$$

Similar to the single-electron case, its exact solution can be written as

$$|\Psi^N(t)\rangle = -i\int_{t_0}^t dt'\, U^N(t, t')V_L^N(t')U_0^N(t', t_0)\Psi_g^N(\mathbf{r}) + U_0^N(t, t_0)|\Psi_g^N\rangle. \tag{1.91}$$

Here the U_0^N and U^N are the N-electron propagators. The former is determined by

$$i\partial U_0^N/\partial t = H_0^N U_0^N, \tag{1.92}$$
$$U^N(t_0, t_0) = 1, \tag{1.93}$$

where H_0^N is the field-free Hamiltonian of the molecule: $H_0^N = H^N - V_L^N$. The latter is the full propagator determined by $i\partial U^N/\partial t = H^N U^N$.

The harmonic dipole reads

$$\begin{aligned}\mathbf{D}(t) &= -i\langle U_0^N(t, t_0)\Psi_g^N(\mathbf{r})|\mathbf{d}|\int_{t_0}^t dt'\, U^N(t, t') \times \\ &\quad \times V_L^N(t')U_0^N(t', t_0)\Psi_g^N(\mathbf{r})\rangle + c.c. \end{aligned} \tag{1.94}$$

Just as in the one-electron case (Eq. 1.13), propagation without the laser field is simple as long as the energy E_g and the wavefunction of the initial state of the neutral molecule or atom are known:

$$U_0^N(t', t_0)\Psi_g^N(\mathbf{r}) = e^{-iE_g(t'-t_0)}\Psi_g^N(\mathbf{r}). \tag{1.95}$$

Finding the full propagator $U^N(t, t')$ is just as hard as solving the multi-electron TDSE.

To simplify the analysis, we will make the following two approximations. First, we shall neglect the correlations between the electrons in the ion and the liberated electron after ionization. In this case, the full propagator factorizes into two independent parts describing the evolution of the continuum electron and the evolution of the ion in the laser field between ionization and recombination: $U^N(t, t') \simeq$

$U^{(N-1)}(t,t')U^e(t,t')$. Second, we will derive the results for short range potentials, just like we did in the single electron case considered above: $U^e(t,t') \simeq U^e_V(t,t')$, and supply the corrections due to Coulomb effects.

One can improve upon these two approximations by including the electron-electron correlations during ionization perturbatively, Walters and Smirnova (2010), and by using the eikonal-Volkov states, Smirnova *et al.* (2008), for the continuum electron, instead of the plane wave Volkov states. The eikonal-Volkov states include the laser field fully, the interaction of the continuum electron with the core in the eikonal approximation, and also take into account the interplay between these two interactions (the so-called Coulomb-laser coupling, Smirnova *et al.* (2007a)).

A consistent approach, which includes both electron-electron correlations and long-range effects in strong field ionization can be developed within the time-dependent analytical R-matrix (ARM) method (Torlina *et al.* (2012)). This method (i) splits the configuration space into the inner and outer region, uses quantum chemistry in the inner region, (ii) the eikonal-Volkov propagation in the outer region,(Smirnova *et al.* (2008)), and (iii) the Bloch operator (Bloch (1957)) to match the solutions in two regions.

Moreover, if we can factorize the dipole response into the usual steps – ionization, propagation, recombination, we can think of improving each of the three steps separately, e.g. by using improved ionization and recombination amplitudes that include the electron-electron correlation beyond the perturbation theory.

Just like in the one-electron formalism considered above, we will introduce the identity resolved on the momentum states of the continuum electron, but now we also have to include the electronic states of the ion [7]:

$$I = \int d\mathbf{p} \sum_n \mathbb{A}|n^{(N-1)} \otimes \mathbf{p}_t^n\rangle\langle n^{(N-1)} \otimes \mathbf{p}_t^n|\mathbb{A}, \tag{1.96}$$

where $\mathbb{A}$ denotes the antisymmetrizing operator.

The harmonic dipole becomes

$$\begin{aligned}\mathbf{D}(t) &= -i\langle\Psi_g^N|\mathbf{d}|\int_{t_0}^t dt'\, e^{iE_g(t-t')} \int d\mathbf{p}\, U^{(N-1)}(t,t')|n^{(N-1)}\rangle \times \\ &\quad \times U^e_V(t,t')|\mathbf{p}_{t'}^n\rangle\langle\mathbf{p}_{t'}^n n^{(N-1)}|V_L^N(t')|\Psi_g^N\rangle + c.c.\end{aligned} \tag{1.97}$$

Note a crucial change compared to the single-channel case (Eq. 1.18): the appearance of the laser-induced dynamics between the bound states of the ion, described by the propagator $U^{(N-1)}(t,t')|n^{(N-1)}\rangle$. This dynamics can be calculated if the dipole couplings, d_{mn}, between all essential states, as well as their eigenenergies, E_n, are known.

Consider, for example, the case of an N_2 molecule with three essential states in the N_2^+ ion, denoted as X, A and B, see Fig.1.11. The time-dependent transition amplitudes $a_{mn}(t,t')$ between the state $n^{(N-1)}$ populated at the moment t' and the state

---

[7] Here we use the field-free states of the ion. If the limited amount of basis states is used, then one should try to find the optimal "laser-dressed" basis.
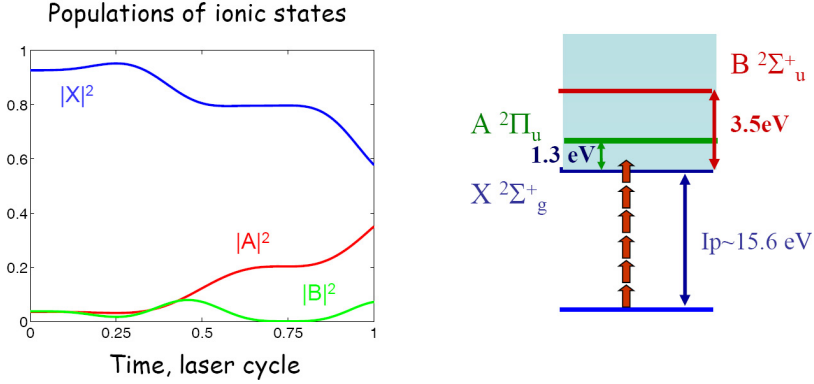
Populations of ionic states

Figure 1.11 Left panel: Sub-cycle dynamics in the N_2^+ ion aligned at $\theta = 50^o$ to the laser field polarization: populations of the field-free ionic states X (blue), A (red), and B (green) in a $I = 0.8 \cdot 10^{14}$ W/cm^2, 800 nm laser field. Right panel: Electronic states of the N_2^+ ion.

$m^{(N-1)}$ at the moment t are given by $a_{mn}(t, t') = \langle m^{(N-1)}|U^{(N-1)}(t, t')|n^{(N-1)}\rangle$. It is a solution of the following system of differential equations:

$$\frac{d(\mathbf{A}^{(n)})}{dt} = [\mathbf{H} + \mathbf{V}(t)]\, \mathbf{A}^{(n)}, \tag{1.98}$$

where, for our three ionic states, the Hamiltonian of the ion is $\mathbf{H} = \begin{pmatrix} E_1 & 0 & 0 \\ 0 & E_2 & 0 \\ 0 & 0 & E_3 \end{pmatrix}$,

with the energies E_n of the three states. The interaction between these three states is described by the matrix of the laser-induced couplings, $V_{mn}(t) = -\mathbf{d}_{mn} \cdot \mathbf{F}(t)$, that is $\mathbf{V}(t) = \begin{pmatrix} 0 & V_{12}(t) & V_{13}(t) \\ V_{21}(t) & 0 & V_{23}(t) \\ V_{31}(t) & V_{32}(t) & 0 \end{pmatrix}$. Finally, $\mathbf{A}^{(n)} = \begin{pmatrix} a_{1n}(t, t') \\ a_{2n}(t, t') \\ a_{3n}(t, t') \end{pmatrix}$ is the vector describing the population amplitudes of all essential ionic states, starting from the state $n^{(N-1)}$ at time t'.

Let us introduce channel specific Dyson orbitals $\Psi_n^D(\mathbf{r}) \equiv \langle n^{(N-1)}|\Psi_g^N(\mathbf{r})\rangle$. These are the overlaps between the N-electron wavefunction of the ground state of the neutral and the $(N-1)$-electron wavefunction of the ionic state $|n^{(N-1)}\rangle$. Let us assume that the dipole operator that starts ionization at the moment t' in Eq. (1.97) acts only on the electron, that will be liberated (i.e. we neglect the exchange-like effects in ionization). In this case, the multielectron dipole $\mathbf{D}_{mn}$, which corresponds to leaving the ion in the state $n^{(N-1)}$ after ionization and then recombination with the ion in the state $m^{(N-1)}$, can be re-written in a form very similar to the one-electron case (Eq. (1.24)):

$$\mathbf{D}^{(mn)}(t) = i \int_{t_0}^t dt' \int d\mathbf{p}\, \mathbf{d}_m^*(\mathbf{p} + \mathbf{A}(t))\, a_{mn}(t, t')\, e^{-iS_n(\mathbf{p}, t, t')} \times$$

$$\times \mathbf{F}(t')\mathbf{d}_n(\mathbf{p} + \mathbf{A}(t')), \tag{1.99}$$

$$\mathbf{d}_n(\mathbf{p} + \mathbf{A}(t)) = \langle \mathbf{p} + \mathbf{A}(t)|\mathbf{d}|\Psi_n^D\rangle,$$

$$\mathbf{d}_m(\mathbf{p} + \mathbf{A}(t)) = \langle \mathbf{p} + \mathbf{A}(t)|\langle n^{(N-1)}|\mathbf{d}|\Psi_g^N\rangle,$$

$$S_n(\mathbf{p}, t, t') = \frac{1}{2}\int_{t'}^{t}[\mathbf{p} + \mathbf{A}(\tau)]^2 d\tau + I_{p,n}(t - t').$$

This expression is remarkably similar to one-electron dipole (1.24). The transformation similar to (1.22) is also valid in this case, yielding

$$\mathbf{D}^{(mn)}(t) = i\int_0^t dt'\int d\mathbf{p}\, \mathbf{d}_m^*(\mathbf{p} + \mathbf{A}(t))\, a_{mn}(t, t')\, e^{-iS(\mathbf{p},t,t')} \times$$
$$\times\Upsilon_n(\mathbf{p} + \mathbf{A}(t')), \tag{1.100}$$
$$\Upsilon_n(\mathbf{p} + \mathbf{A}(t)) = \left[\frac{[\mathbf{p} + \mathbf{A}(t)]^2}{2} + I_{p,n}\right]\langle \mathbf{p} + \mathbf{A}(t)|\Psi_n^D\rangle,$$

where $I_{p,n}$ is the ionization potential to the state n of the ion and the matrix $a_{mn}(t, t')$ is calculated while setting E_n to zero.

The total harmonic signal results from the coherent superposition of the dipoles $\mathbf{D}_{mn}$ associated with each ionization-recombination channel:

$$\mathbf{D}(t) = \sum_{m,n}\mathbf{D}^{(mn)}(t). \tag{1.101}$$

Substantial sub-cycle transitions, such as those shown in Fig. 1.11 for the N_2^+ ion in typical experimental conditions, have a crucial impact on the harmonic radiation. They lead to the appearance of the cross-channels in HHG (the off-diagonal elements $\mathbf{D}^{(mn)}$ for $m \neq n$ in Eq. (1.101)) since the state of the ion changes between the ionization and the recombination, see Fig. 1.12. These channels are indeed substantial in high harmonic generation from the N_2 molecules, see Mairesse *et al.* (2010), as illustrated in Fig. 1.11.

In the recent literature on high harmonic generation one can often come across a rather loose language, which refers to different ionization and recombination channels as associated with different Hartree-Fock molecular orbitals. This language should not be taken literally as a statement on the applicability of the Hartree-Fock picture and on the physical reality of the Hartree-Fock orbitals as observable physical quantities. Loosely speaking, removing an electron from the highest occupied molecular orbital (HOMO) creates the ion in the ground state. Removing an electron from one of the lower lying orbitals (e.g. HOMO-1, HOMO-2) creates the ion in one of its excited states. Thus, the reference to the orbitals should only be understood as a language for describing ionization and recombination channels associated with different multielectron states of the ion – and those are physically relevant and observable. In the orbital language, electron removal from an orbital creates a hole in this orbital. The laser induced dynamics in the ion, moves the hole between the orbitals in the time window between ionization and recombination, see Fig. 1.12.

Application of the saddle point method in each channel leads to the following half-
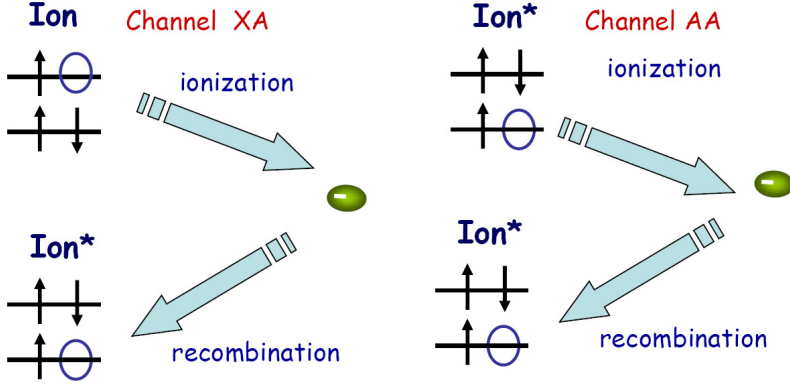
Figure 1.12 Left panel: Cross-channel in HHG associated with ionization from and recombination to different orbitals. This channel is due to real excitations induced by the laser field between ionization and recombination. Right panel: Diagonal channel in HHG associated with ionization from and recombination to the same orbital.

cycle dipole for the given ionization – recombination channel:

$$\mathbf{D}^{(j,mn)}(t) = \mathbf{a}^m_{rec}(\mathbf{p}_s, t) a^{mn}_{prop}(\mathbf{p}_s, t, t_i^{(j)}) a^n_{ion}(\mathbf{p}_s, t_i^{(j)}), \tag{1.102}$$

$$a^n_{ion}(\mathbf{p}_s, t_i) = \left[\frac{2\pi}{S''_{t_i,t_i}} \right]^{1/2} e^{-iS(\mathbf{p}_s, t_i^{'(j)}, t_i^{(j)})} \Upsilon_n(\mathbf{p}_s + \mathbf{A}(t_i^{(j)})), \tag{1.103}$$

$$a^{mn}_{prop}(\mathbf{p}_s, t, t_i) = \frac{(2\pi)^{3/2}}{(t-t_i)^{3/2}} e^{-iS(\mathbf{p}_s, t, t_i^{'(j)})} a_{mn}(t, t_i^{(j)}), \tag{1.104}$$

$$\mathbf{a}^m_{rec} = \mathbf{d}^*_m(\mathbf{p}_s + \mathbf{A}(t)). \tag{1.105}$$

Neglecting the sub-cycle dynamics in the prefactor of $a^n_{ion}(\mathbf{p}_s, t_i)$ we can substitute Eq. (1.103) by the following expression, which includes the Coulomb effects in ionization (the sub-cycle Coulomb effects see Torlina and Smirnova (2012)):

$$a^n_{ion}(\mathbf{p}_s, t_i) = 2 \left(\frac{2\kappa^3}{F} \right)^{\frac{Q}{\kappa}} \sqrt{\frac{-\tilde{\gamma}\omega}{\kappa\sqrt{1+\tilde{\gamma}^2}}} e^{-iS(\mathbf{p}_s, t_i', t_i)} \Upsilon_n(\mathbf{p}_s + \mathbf{A}(t_i)). \tag{1.106}$$

A term similar to Υ_n also arises within the time-dependent analytical R-matrix approach applied to multi-channel strong field ionization Torlina *et al.* (2012). However in Torlina *et al.* (2012), the radial integration is removed due to the use of the Bloch operator. Thus in Torlina *et al.* (2012), the pole in Υ_n does not arise even when the long-range potential is taken into account. Function $\Upsilon_n(\mathbf{p}_s + \mathbf{A}(t_i))$ encodes the angular structure of the Dyson orbital in the asymptotic region, which is more complex than the one arising in the asymptotic of the atomic wave-function (1.56) leading to Eq. (1.58). The simple expressions for the asymptotic of the Dyson orbital for small molecules can be found in Murray *et al.* (2011).

Here, we have considered the harmonic dipole on the real time axis. Note that the propagation amplitude is modified compared to the one in the one-electron case

(Eq. 1.72) to include the laser – induced dynamics in the ion $a_{mn}(t)$. The full dipole for each ionization-recombination channel is the sum over the different half-cycles and the harmonic spectrum results from the FFT of the full dipole $\mathbf{D}_{mn}(N\omega)$:

$$\mathbf{D}^{(mn)}(t) = \sum_j \mathbf{D}^{(j,mn)}(t), \tag{1.107}$$

$$\mathbf{D}^{(mn)}(N\omega) = \int dt\, \mathbf{D}^{(mn)}(t)e^{iN\omega t}. \tag{1.108}$$

The complete harmonic response is obtained by adding coherently the contributions of all ionization – recombination channels.

1.9
Outlook

Having factorized the dipole, we can use improved amplitudes for each step. These are the key components of the current theoretical work in high harmonic spectroscopy of molecules.

Improving ionization. Improved ionization amplitudes can be taken from semi-analytical and/or numerical approaches. The task is to define the function $\Upsilon(\mathbf{p} + \mathbf{A}(t))$ for a realistic system and include long-range and polarization (Sukiasyan *et al.* (2010)) effects. For example, one can use the results of Murray *et al.* (2011), where the ionization amplitude is represented as:

$$\widetilde{a}^n_{ion}(\mathbf{p}_s, t_i) = \mathbb{R}_{\mathfrak{lm}}(I_p, F)e^{-iS(\mathbf{p}_s, t'_i, t_i)}. \tag{1.109}$$

The exponent describes the sub-cycle dynamics of strong-field ionization, i.e. is the same as for the atomic case and a short-range potential. The prefactor $\mathbb{R}_{\mathfrak{lm}}(I_p, F)$ accounts for the influence of the core potential and the shape of the initial state on the ionization rate. For atoms, this prefactor has been derived in the seminal papers of Perelomov, Popov and Terent'ev (see Perelomov *et al.* (1966, 1967); Perelomov and Popov (1967); Popov *et al.* (1968)) and improved in Popruzhenko *et al.* (2008). A simple recipe for incorporating their results into the sub-cycle ionization amplitudes can be found in Yudin and Ivanov (2001). Fully consistent treatment of long-range, polarization and orbital effects can be developed within the time-dependent analytical R-matrix (ARM) approach, see Torlina and Smirnova (2012); Torlina *et al.* (2012).

Improving propagation. In addition to the dynamics in the molecular ion, including the laser-induced transitions between different ionic states, the second most important modification of the propagation amplitudes is the incorporation of possible transverse nodal structure in the continuum wavepackets. The nodal planes in the continuum wavepacket arise during tunnelling from bound states. For example, in the CO_2 molecule, the HOMO and the corresponding Dyson orbital have nodal planes parallel and perpendicular to the molecular axis. Consequently, in the case of tunnel ionization with the molecular axis aligned parallel to the polarization of the ionizing field, the nodal plane will not only reduce the ionization rate, but will also

be imprinted on the shape of the electronic wavepacket that emerges after ionization. Propagation between ionization and recombination will lead to the spreading of the wavepacket, but it will not remove the presence of the node as the wavepacket returns to the core Smirnova *et al.* (2009a,c,b). Clearly, this aspect of propagation is important for the recombination amplitude.

Consider, for example, ionization from a state with angular momentum $L = 1$. Its projection on the laser polarization is either $L_z = 0$ (no nodal plane along the electric field) or $L_z = 1$ (nodal plane along the electric field). After tunnelling, in the plane orthogonal to the laser polarization, in the momentum space the continuum wavepackets are proportional to $\left(\frac{p_\perp}{\kappa}\right)^m$, (see Eq.1.62 or 1.66):

$$\Psi_{L_z=0}(p_\perp) \propto e^{-\frac{p_\perp^2}{2}\tau},$$

$$\Psi_{L_z=1}(p_\perp) \propto \frac{p_\perp}{\kappa} e^{i\phi_p} e^{-\frac{p_\perp^2}{2}\tau}, \tag{1.110}$$

where $\tau = \text{Im}(t_i)$, $\kappa = \sqrt{2I_p}$, and ϕ_p is the angle between $p_\perp$ and the x-axis. As we can see, the presence of the nodal plane for $L_z = 1$ leads to the additional term $p_\perp/\kappa$. We now propagate these wavepackets until the recombination time t_r. Fourier transforming back into the coordinate space, in the plane orthogonal to the laser polarization, we get

$$\Psi_{L_z=0}(\rho) \propto e^{-\frac{\rho^2}{2(t_r-t_i)}}$$

$$\Psi_{L_z=1}(\rho) \propto \frac{\rho}{\kappa(t_r-t_i)} e^{i\phi} e^{-\frac{\rho^2}{2(t_r-t_i)}} \tag{1.111}$$

where ρ is the transverse radial coordinate and ϕ is the angle between the radial vector and the x-axis. Recalling that $x = \rho\cos\phi$, we see that if we combine the $L_z = \pm1$ states to form the real-valued spherical harmonic p_x, the presence of the nodal plane effectively changes the dipole operator $\mathbf{d}$ to $\mathbf{d} \cdot x/(\kappa(t_r - t_i))$. In Smirnova *et al.* (2009a,c,b) such modifications of recombination operators has been used to account for the appearance of nodal planes.

In most experiments with molecular HHG to-date, the alignment distribution is rather broad. Even if the molecular ensemble is, on average, aligned parallel to the laser polarization, for most molecules the characteristic alignment angle would be sufficiently different from that associated with the nodal plane. In this case, the relative importance of the nodal planes in recombination is reduced. However, for well-aligned molecular ensembles this would become a significant factor.

Improving recombination. The recombination step can be significantly improved beyond the SFA, if one uses the recombination dipoles $\mathbf{d}_m^*(\mathbf{p}_s + \mathbf{A}(t))$ calculated using ab-initio approaches. For example, the quantitative rescattering theory (see Lin *et al.* (2010)) relies on using the Schwinger variational method to calculate the field-free recombination matrix elements. Alternatively, one can use the R-matrix approach (see Harvey and J. (2009); Harvey *et al.* (2012)). Both allow one to incorporate the full complexity of the recombination process, including the channel coupling due to the electron-electron correlation and automatically include the exchange effects in

recombination Gordon and Santra (2006); Patchkovskii *et al.* (2006); **?**. The drawback of these methods, at the moment, is the absence of the laser field in the calculations of the recombination amplitudes. This approximation breaks down in case of a structured continuum Patchkovskii *et al.* (2012), common for many molecules. The impact of the IR field on such continuum states has been recently demonstrated experimentally Ott *et al.* (2013), substantiating the prediction of Patchkovskii *et al.* (2012). In the approach described by Smirnova *et al.* (2009a), the eikonal-Volkov approximation for the continuum states was used to obtain improved dipoles in the single-channel approximation with exchange. The eikonal-Volkov approximation fully includes the interaction of the continuum electron with the laser field, but the interaction with the core potential is only included in the eikonal approximation, and the correlation-induced channel coupling is neglected. Improving the recombination amplitudes to account for all these effects – the channel coupling due to the electron-electron correlation, the core potential, and the laser field, is one of the key theoretical challenges today.

With each of the three steps in the harmonic response improved, the original SFA-based theory turns from purely qualitative into a little more realistic. The separation of the three steps, crucial for our ability to improve each of them separately, benefits from the high intensity of the driving field and the large oscillation amplitude of the active electron. The high field intensity also lies at the heart of the main difficulties in building an adequate theoretical description. Nevertheless, the effort is worth the investment: the combination of attosecond temporal and Angstrom spatial resolution is extremely valuable. High harmonic spectroscopy appears to be well suited for tracking the multielectron dynamics induced by the ionization process.

It is very attractive to replace the ionization step induced by the IR field with the one-photon ionization induced by a controlled attosecond XUV pulse, phase-locked to the strong IR field (see Schafer *et al.* (2004)). The latter would drive the continuum electron. Such an arrangement should allow one to move from dealing with outer valence electrons to dealing with inner valence and deeper lying electrons. This appears to be an exciting regime for tracking the hole dynamics (Lunnemann *et al.* (2008)) initiated by inner-valence or deeper ionization. Importantly, for deeply bound orbitals, the effect of the IR driving field on the core-rearrangement and the hole dynamics should be substantially less than for the outer-valence electrons.

High harmonic spectroscopy helps to record the relative phases between different ionization channels, which provide information about electron rearrangement during ionization and define the initial conditions for the hole migration both in the inner valence (Lunnemann *et al.* (2008)) and outer valence (Smirnova *et al.* (2009a)) shells. These initial conditions are sensitive to the frequency, intensity and duration of the ionizing pulse, opening opportunities for controlling hole migration and, possibly, related chemical reactions Weinkauf *et al.* (1997).

1.10
Acknowledgements

We are grateful to Maria Richter for reading the manuscript and suggesting many important corrections, Szczepan Chelkowski and Thomas Schultz for useful comments, and Felipe Morales for his help in preparing the manuscript. We thank Pascal Salières and Alfred Maquet for encouraging us to undertake this project. Finally, we acknowledge the stimulating atmosphere of the KITPC workshop "Attosecond Science - Exploring and Controlling Matter on Its Natural Time Scale" in Beijing.

1.11
Appendix A: Supplementary derivations

In this Section we prove that the transformation (1.22):

$$\int_{t_0}^{t} dt' \, e^{-iS(\mathbf{p},t,t')} \, \mathbf{F}(t') \, \mathbf{d}(\mathbf{p} + \mathbf{A}(t')) = \tag{1.112}$$

$$= \int_{t_0}^{t} dt' \, e^{-iS(\mathbf{p},t,t')} \Upsilon(\mathbf{p} + \mathbf{A}(t')),$$

$$\Upsilon(\mathbf{p} + \mathbf{A}(t')) = \left[\frac{(\mathbf{p} + \mathbf{A}(t'))^2}{2} + I_p \right] \langle \mathbf{p} + \mathbf{A}(t') | g \rangle, \tag{1.113}$$

is applicable in case of high harmonic generation. By definition

$$\int_{t_0}^{t} dt' \, e^{-iS(\mathbf{p},t,t')} \, \mathbf{F}(t') \, \mathbf{d}(\mathbf{p} + \mathbf{A}(t')) \equiv \tag{1.114}$$

$$\equiv e^{-iI_p t} \int_{t_0}^{t} dt' \langle \Psi_{\mathbf{p}}^{V}(t';t) | - V_L | g(t') \rangle.$$

Adding and subtracting the kinetic energy operator $\widehat{\frac{\mathbf{p}^2}{2}}$ (Becker *et al.* (2002b), Gribakin and Kuchiev (1997)) we obtain:

$$\int_{t_0}^{t} dt' \langle \Psi_{\mathbf{p}}^{V}(t';t) | - \widehat{\frac{\mathbf{p}^2}{2}} - V_L + \widehat{\frac{\mathbf{p}^2}{2}} | g(t') \rangle \equiv \tag{1.115}$$

$$\equiv \int_{t_0}^{t} dt' \left\{ i \frac{\langle \partial \Psi_{\mathbf{p}}^{V}(t';t) |}{\partial t'} | g(t') \rangle + \left[\frac{(\mathbf{p} + \mathbf{A}(t'))^2}{2} \right] \langle \Psi_{\mathbf{p}}^{V}(t';t) | g(t') \rangle \right\}. \tag{1.116}$$

Here we have used that $-i \frac{\langle \partial \Psi_{\mathbf{p}}^{V}(t';t) |}{\partial t'} = \left[\widehat{\frac{\mathbf{p}^2}{2}} + V_L \right] \langle \Psi_{\mathbf{p}}^{V}(t';t) |$. Integrating by parts the first term in Eq.(1.116) we obtain:

$$\int_{t_0}^{t} dt' \, i \frac{\langle \partial \Psi_{\mathbf{p}}^{V}(t';t) |}{\partial t'} | g(t') \rangle = \tag{1.117}$$

$$= -i \int_{t_0}^{t} dt' \langle \Psi_{\mathbf{p}}^{V}(t';t) | \frac{\partial | g(t') \rangle}{\partial t'} + \langle \Psi_{\mathbf{p}}^{V}(t';t) | g(t') \rangle |_{t_0}^{t}. \tag{1.118}$$

The transformation (1.112) can be recovered using $i\frac{\partial|g(t')\rangle}{\partial t'} = -I_p|g(t')\rangle$ and taking into account that the boundary term $\langle\Psi_\mathbf{p}^V(t';t)|g(t')\rangle|_{t_0}^t$ does not contribute to the high harmonic dipole. Indeed the contribution of the boundary term to high harmonic dipole is:

$$\int d\mathbf{p}\, \mathbf{d}^*(\mathbf{p}+\mathbf{A}(t)) \left[\langle\Psi_\mathbf{p}^V(t;t)|g(t)\rangle - \langle\Psi_\mathbf{p}^V(t_0;t)|g(t_0)\rangle \right] = \tag{1.119}$$

$$= \int d\mathbf{p}\, \langle g(t)|\hat{\mathbf{d}}|\Psi_\mathbf{p}^V(t;t)\rangle\langle\Psi_\mathbf{p}^V(t;t)|g(t)\rangle - \tag{1.120}$$

$$- \int d\mathbf{p}\, \langle g(t)|\hat{\mathbf{d}}|\Psi_\mathbf{p}^V(t;t)\rangle\langle\Psi_\mathbf{p}^V(t_0;t)|g(t_0)\rangle. \tag{1.121}$$

The term (1.120) is equal to zero, the term (1.121) tends to zero when $t_0 \to -\infty$. Indeed,

$$\int d\mathbf{p}\, \langle g(t)|\hat{\mathbf{d}}|\Psi_\mathbf{p}^V(t;t)\rangle\langle\Psi_\mathbf{p}^V(t;t)|g(t)\rangle = \langle g(t)|\hat{\mathbf{d}}|g(t)\rangle = 0, \tag{1.122}$$

while the second term (1.121) is:

$$\int d\mathbf{p}\, \langle g(t)|\hat{\mathbf{d}}|\Psi_\mathbf{p}^V(t;t)\rangle\langle\Psi_\mathbf{p}^V(0;t)|g(0)\rangle = \tag{1.123}$$

$$= \int d\mathbf{p}\, e^{-i\frac{1}{2}\int_{t_0}^t d\tau[\mathbf{p}+\mathbf{A}(\tau)]^2} \langle g(t)|\hat{\mathbf{d}}|\mathbf{p}+\mathbf{A}(t)\rangle\langle\mathbf{p}|g\rangle. \tag{1.124}$$

This term corresponds to the projection of the ground state onto the basis of plane waves at $t_0 \to -\infty$ followed by recombination of the resulting oscillating wave-packet back to the ground state at time t. Spreading of the free electron wave-packet over infinite time $(t - t_0) \to +\infty$ makes this projection negligible.

1.12
Appendix B: The saddle point method

The saddle point method is one of the key techniques in the analytical strong-field theory. It is an asymptotic method, which allows one to analytically evaluate the integrals from highly oscillating functions, such as the integral in Eq. (1.19).

1.12.1
Integrals on the real axis

How would one calculate the following integral,

$$I = \int_a^b f(x)e^{\lambda h(x)}\,dx \tag{1.125}$$

for some smooth functions $f(x)$ and $h(x)$, without knowing much about them, or if they look ugly and complicated? All we know is that they are real-valued functions on the real axis x.

In general, one could think that there is not much one can do. Fortunately, this is not the case if the positive and real λ is large, $\lambda \gg 1$ – then, the integral can be calculated.

1.12.1.1 Contribution of the end points

The first idea that comes to my mind when looking at such an integral is to try integration by parts. This approach works just fine under certain circumstances, see below. The first stumbling block meets you right at the gate: how does one integrate by parts if both $h(x)$ and $f(x)$ are unknown?

The trick is simple:

$$
\begin{aligned}
I &= \int_a^b f(x)e^{\lambda h(x)}dx \\
&= \int_a^b dx \frac{f(x)}{\lambda h'(x)} \lambda h'(x) e^{\lambda h(x)} \\
&= \frac{1}{\lambda} \frac{f(x)}{h'(x)} e^{\lambda h(x)}|_a^b - \frac{1}{\lambda} \int_a^b dx e^{\lambda h(x)} \left[\frac{d}{dx} \left(\frac{f(x)}{h'(x)} \right) \right].
\end{aligned}
\tag{1.126}
$$

We started with an integral that did not have a small parameter $1/\lambda$ in front. Now we have two terms: the first comes from the contributions at the end points. The second term is another integral, now with a small parameter in front. Dealing with it in the same way as with the original integral, we will get terms proportional to $1/\lambda^2$, and so on.

Thus, we conclude that the main contribution to the integral comes from the end points, and is given by the first term:

$$
\begin{aligned}
I &= \int_a^b f(x)e^{\lambda h(x)}dx \\
&= \frac{1}{\lambda} \left[\frac{f(b)}{h'(b)} e^{\lambda h(b)} - \frac{f(a)}{h'(a)} e^{\lambda h(a)} \right] + O(\lambda^{-2}).
\end{aligned}
\tag{1.127}
$$

This result is applicable unless there is a problem with the second term in Eq. (1.126) – the integral

$$
-\frac{1}{\lambda} \int_a^b dx e^{\lambda h(x)} \left[\frac{d}{dx} \left(\frac{f(x)}{h'(x)} \right) \right].
\tag{1.128}
$$

The problem arises if $h'(x) = 0$ somewhere between the two end points of the integral. What do we do then? Obviously, the points where $[f(x)/h'(x)]$ diverges can bring major contributions to the integral.

Given that $\lambda \gg 1$, the way the exponential function changes between a and b is most important. The first possibility is $h' \neq 0$ in the integration interval. Then, the integral is accumulated at the end points, and the end point where $h(x)$ is larger dominates. In general, for an exponential function $e^{\lambda h(x)}$ the main contribution to the integral will come from the region where it reaches its maximum value – and hence where $h'(x) = 0$.
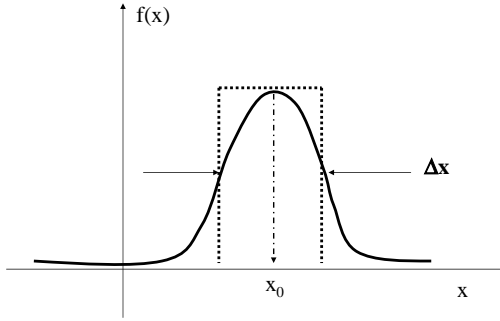
Figure 1.13 Integral from a bell-shaped curve with a maximum at x_0 and a width of Δx.

Suppose that, somewhere between a and b, the derivative $h' = 0$. If the function $h(x)$ has a minimum, the contribution of this minimum won't be competitive with the contributions from the end points (remember that λ is large and positive). But if it has a maximum, then the main contribution to the integral comes from the region near the maximum. The way to handle this situation is described in the next section.

1.12.1.2 The Laplace Method

Let us consider an integral from a function $f(x)$ shown in Fig. 1.13. The function is bell-shaped, has a maximum at the point x_0, where its first derivative is, of course, equal to zero, and quickly falls off to each side of x_0.

Calculation of this integral is very simple - all we need is to find the effective width Δx of the bell-shaped curve, and then the integral is

$$I = \int_{-\infty}^{\infty} f(x)dx = f(x_0)\Delta x. \tag{1.129}$$

Let us first try some simple estimates of the width Δx. In order to do it, we expand $f(x)$ around x_0 in a Taylor series, remembering that the first derivative is zero at this point:

$$f(x) \approx f(x_0) + \frac{1}{2}f''(x_0)(x - x_0)^2 = f(x_0) - \frac{1}{2}|f''(x_0)|(x - x_0)^2. \tag{1.130}$$

Notice that I have explicitly used the fact that the second derivative at the local maximum is negative.

A potential candidate for the width Δx is the full width at half maximum (FWHM). The half-width $\Delta x/2$ at each side is given by

$$f(x_0) - \frac{1}{2}|f''(x_0)|(\Delta x/2)^2 = f(x_0)/2. \tag{1.131}$$

This gives us $\Delta x = \sqrt{4f_0/|f''|}$.

A more accurate calculation of the required width comes from the following trick, which will also smoothly bring us into the saddle point method

$$I = \int f(x)dx = \int e^{\ln f(x)}dx. \tag{1.132}$$

This transformation allows us to reduce the integral to a familiar Gaussian form. We proceed by expanding $\ln f(x)$ in a Taylor series, remembering that $f'(x_0) = 0$ and $f''(x_0) = -|f''(x_0)|$:

$$I = \int e^{\ln f(x)}dx \simeq \int e^{\ln f(x_0) - \frac{|f''(x_0)|}{f(x_0)}\frac{(x-x_0)^2}{2}}dx. \tag{1.133}$$

Recalling that the integral from a Gaussian is

$$\int_{-\infty}^{\infty} e^{-ax^2}dx = \sqrt{\pi/a}, \tag{1.134}$$

and setting the limits of our integral to $\pm\infty$, we get the final answer

$$I = f(x_0)\sqrt{2\pi f(x_0)/|f''(x_0)|}. \tag{1.135}$$

As you can see, the width Δx turned out to be pretty close to the FWHM.

1.12.1.3 **Saddle point method: the steepest descent in a complex plane**

We now move to the *saddle point method* which is used for integrals of complex-valued functions:

$$I = \int_C e^{\lambda f(z)}dz. \tag{1.136}$$

where λ is large and positive, and the rest is hidden in $f(z)$. The integral is to be taken over a contour C, and the only good thing about this contour is that its ends, somewhere far away from the place of action, do not contribute to the value of the integral.

There are assumed to be no poles, so that we are allowed to deform the contour C as we wish. The key of the steepest descent is a clever modification of the integration contour.

First, note that a complex function $f(z)$ has a real part and an imaginary part, $f(z) = u(z) + iv(z) \equiv u(x, y) + iv(x, y)$, where x and y are the real and the imaginary parts of z, $z = x + iy$.

Let us now look at the integral more closely and recall the previous section, where the integration was based on expanding the function around a maximum and reducing the integrand to a Gaussian. In our case we have a function $\exp(\lambda u + i\lambda v)$ that changes its absolute value very rapidly due to the λu part. It also oscillates rapidly due to the λv part. The trick of the steepest descent is to modify the contour of integration in such a way that it will go through a place where the real part u climbs to a maximum

along the contour and then quickly falls, while the imaginary part v stays constant along the same contour, freezing any fast oscillations.

It may not be obvious at first glance that such a modification of the contour is possible. But it is.

We start in a manner entirely analogous to the previous section. Let us assume that the function $f(z)$ has a zero derivative at the point $z_0 = x_0, y_0$, where x_0 and y_0 are coordinates in the complex plane; the point z_0 lies somewhere between the left and the right ends of the contour C.

If $f_z(z_0) = 0$, then both the real and the imaginary parts of f must have zero derivatives there:

$$u_x = v_x = 0, \quad v_y = u_y = 0. \tag{1.137}$$

Thus, not only at z_0 the absolute magnitude of our function goes through an extremum, but also the oscillating part is stationary. Another important observation is that the gradients of the two functions, ∇u and ∇v, are always orthogonal to each other:

$$\nabla v \cdot \nabla u = u_x v_x + u_y v_y = 0. \tag{1.138}$$

This is the consequence of the Cauchy-Riemann conditions:

$$u_x = v_y, \quad v_x = -u_y. \tag{1.139}$$

The gradient points into the direction for which the function changes. If we move along the gradient of u, following the path of its steepest rise and fall through the point z_0, we are also moving orthogonal to the gradient of v. Thus, v will stay constant, and fast oscillations are frozen. We see that the desired modification of the contour is indeed possible.

How should the landscape of $u(x, y)$ look like? Due to the same Cauchy-Riemann conditions the functions u and v can only have *saddle points* at z_0:

$$u_{xx} + u_{yy} = 0, \quad v_{xx} + v_{yy} = 0. \tag{1.140}$$

Real mountain peaks, which go down in all directions, only happen at singularities, and we decided that there would be no singularities in $f(z)$.

Therefore, the landscape of the function u around the point z_0 must look something like shown in Fig. 1.14.

All we have to do now is to find the correct path of the *steepest descent through the saddle point*, such that u will rise as quickly as possible as we approach the saddle point and then decrease as quickly as possible as we leave the saddle point. The Cauchy-Riemann conditions promise us that, while we are at it, v will stay constant.

Let us expand $f(z)$ in a Taylor series around z_0, remembering that $f'(z_0) = 0$:

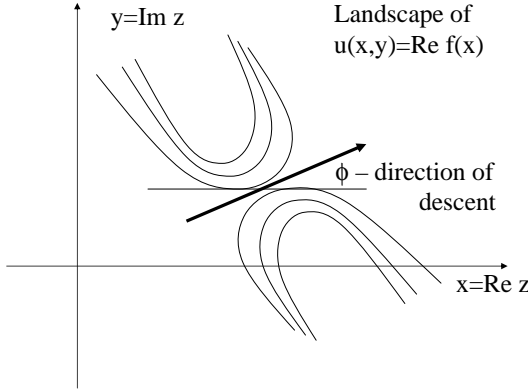$$f(z) \approx f(z_0) + \frac{1}{2} f''(z_0)(z - z_0)^2. \tag{1.141}$$

Figure 1.14 Saddle point method. The landscape of $u(x, y) = \mathrm{Re}f(z)$ around the point z_0 where $f' = 0$.

Of course, $f''(z_0)$ is a complex number, which we will denote as $f''(z_0) = \alpha \exp(i\theta)$. If our path traverses the saddle point at some angle ϕ, then $z - z_0 = \rho \exp(i\phi)$ and

$$\frac{1}{2}f''(z_0)(z - z_0)^2 = \frac{1}{2}\alpha\rho^2 e^{i(\theta+2\phi)}. \tag{1.142}$$

Now, the simple trick is to choose the angle ϕ properly – we set

$$e^{i(\theta+2\phi)} = -1 \tag{1.143}$$

and keep the angle ϕ given by the above condition fixed, changing only ρ, so that $dz = d(z - z_0) = \exp(i\phi)d\rho$.

If we do this, the integral along such a path will look as

$$I = e^{\lambda f(z_0)}e^{i\phi}\int_{C'} e^{-\lambda\alpha\frac{\rho^2}{2}}\,d\rho, \tag{1.144}$$

where the deformed contour C' is going through the saddle point as a straight line at an angle ϕ. Note that, indeed, there are no oscillations along such path, and the real integrand decays as a Gaussian.

The integration limits are now extended to plus and minus infinity and the integral is done:

$$I = e^{\lambda f(z_0)}e^{i\phi}\sqrt{\frac{2\pi}{\lambda\alpha}}. \tag{1.145}$$

Recall that $\alpha \equiv |f''(z_0)|$.

At this point we are almost done, but three important remarks are still in order.

First, there is ambiguity in the definition of the direction ϕ from $\exp(i(\theta + 2\phi)) = -1$. Indeed, the total angle $\theta + 2\phi$ could be both plus and minus π. Thus, formally, without looking at the landscape shown in Fig. 1.14, we have a choice of two ϕ:

$$\phi_1 = -\theta/2 + \pi/2, \quad \phi_2 = -\theta/2 - \pi/2. \tag{1.146}$$

The whole idea of the method is to choose such a direction that you never have to cross the 'mountains' in the landscapes of $u(x, y)$ and $v(x, y)$. You should choose the direction (deforming the contour C) that takes you from the valley, through the saddle point, into another valley. Otherwise, you will also have to include the contributions of the 'mountains' into the integral. Usually, it is the first choice that works, but one should take a look at the landscape and check. The wrong option will go in an obviously wrong way, crossing into the tops of the mountains rather than staying all the way in the valley and smoothly climbing to the saddle. We shall see an example of it in the next section.

Second, if there are several saddle points, i.e. $f(z)$ has many points where its derivative is zero, the integral will be the sum of the contributions from all these points. Then the individual phases ϕ for each saddle point become very important.

Third, there is a modification of the prefactor when dealing with multi-dimensional integrals:

$$I = \int_C e^{\lambda f(z)} dz, \tag{1.147}$$

$$I \simeq \left(\frac{2\pi}{\lambda}\right)^{n/2} e^{\lambda f(z_0)} \frac{1}{\sqrt{-f_{zz}(z_0)}}, \tag{1.148}$$

where f_{zz} is the Hessian matrix (the matrix of the second derivatives of the function f).

1.12.2
Stationary phase method

The stationary phase method is a simple application of the saddle point method to a function with a purely imaginary phase:

$$I = \int g(x) e^{i\lambda f(x)} dx, \tag{1.149}$$

where $g(x)$ is a benign, very slowly changing function which does not do much - just makes sure that the integrand goes to zero at infinity. The constant λ is again real and positive, the integral is supposed to be performed along the real axis and the function $f(x)$ is purely real on the real axis. Intuitively, it is clear that if the function $\exp(i\lambda f(x))$ is oscillating very quickly, its integral averages to zero unless there are some points where the oscillations freeze. These areas are the regions where the
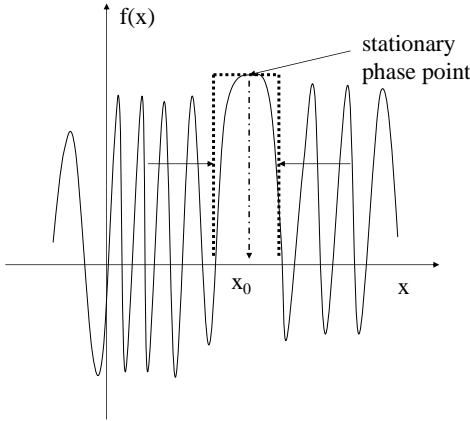
Figure 1.15 Stationary phase method. The integral comes from the area where the integrand does not oscillate as much.

phase of the oscillation, $f(x)$, stays nearly constant, i.e. areas around the point where the derivative turns to zero, $f' = 0$, see Fig. 1.15.

The problem can be turned into that studied in the previous section. Again, suppose that the derivative $f' = 0$ at some point x_0. We use the same Taylor expansion around this point and denote $x - x_0$ as, say, ξ. The integral is approximated as

$$I = g(x_0)e^{i\lambda f(x_0)} \int e^{i\lambda f''(x_0)\frac{\xi^2}{2}} d\xi \tag{1.150}$$

and we will assume that $f'' = \alpha > 0$ (f is a real-valued function and x_0 is on the real axis, hence f'' is real). The case $f'' < 0$ is handled in an identical manner.

Calculation of the integral

$$\int e^{i\lambda\alpha\frac{\xi^2}{2}} d\xi \tag{1.151}$$

follows the exact prescription of the saddle point method. Obviously, the phase θ of the second derivative (see previous section) is $\theta = \pi/2$ (i.e. $i\alpha = \alpha\exp(i\pi/2)$) and the contour of integration has to be turned at an angle ϕ to the real axis, such that $\theta + 2\phi = \pm\pi$. This yields the two possible choices of ϕ: $\phi = +\pi/4$ and $\phi = -3\pi/4$; the answer for the integral is:

$$I = g(x_0)e^{i\lambda f(x_0)}\sqrt{\frac{2\pi}{\alpha\lambda}}e^{i\phi}. \tag{1.152}$$

To find the correct choice of ϕ, one has to look at the landscape of $u(x,y) = \text{Re}(iz^2) = -2xy$. The landscape is shown in Fig. 1.16. The correct choice is obviously the first one, $\phi = +\pi/4$, the second would mean that the contour has to be
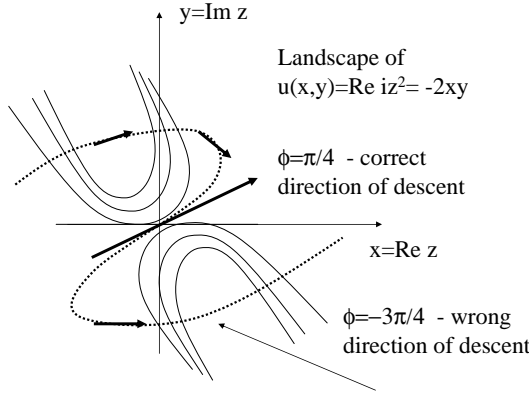
Figure 1.16 Stationary phase method. Correct and incorrect paths of the steepest descent for $f(z) = iz^2$.

deformed as shown in Fig. 1.16 with the dashed line, going through high mountains on the way to the saddle to cross it in the opposite direction of $\phi = -3\pi/4$.

So, the final answer is

$$I = g(x_0)e^{i\lambda f(x_0)}\sqrt{\frac{2\pi}{\alpha\lambda}}e^{i\pi/4}. \tag{1.153}$$

1.13
Appendix C: Treating the cut-off region: regularization of the divergent stationary phase solutions

In this subsection we briefly outline the idea of the so-called uniform approximation - one of the approaches for handling the merging stationary points. The regularization involves two steps. First, we need to find a specific real return time $t_r = t_{r0}$ and the associated $t_i = t_{i0}$, $p_s = p_{s0}$, such that $\partial^2 S(t_{r0}, t_{i0}, p_{s0})/\partial t^2 = 0$. In practice, one can simply pick the real return time corresponding to the cut-off energy. The next step requires the expansion of the total action in Eq. (1.21) around $t = t_{r0}$ in a Taylor series up to the third order:

$$S(t, t_{i0}, p_{s0}) = S(t_{r0}) + (t - t_{r0})S'_{tt} + \frac{(t - t_{r0})^2}{2}S''_{tt} + \frac{(t - t_{r0})^3}{6}S'''_{ttt}, \tag{1.154}$$

where all the derivatives of $S(t, t_{i0}, p_{s0})$ are taken at t_{r0}. Finally, one substitutes the expansion (1.154) into the harmonic dipole,

$$D(N\omega) \propto \int_{-\infty}^{\infty} dt e^{iN\omega t} e^{-iS(t, t_{i0}, p_{s0}) + iN\omega t} + c.c., \qquad (1.155)$$

and uses the Airy function

$$\int_{-\infty}^{\infty} dt \cos(at^3 \pm xt) \equiv \frac{\pi}{(3a)^{1/3}} Ai\left[\frac{\pm x}{(3a)^{1/3}}\right]. \qquad (1.156)$$

Now we introduce the 'cut-off harmonic number' N_0 and the distance from the cut-off $N = N - N_0$:

$$N_0\omega = E_{rec}(t_{r0}) + I_p, \qquad (1.157)$$

here $E_{rec}(t_{r0}) = p_{s0} + A(t_{r0})$ is the re-collision energy at time t_{r0}, and N_0 does not have to be integer. The dipole near the cut-off is expressed via the Airy function:

$$\int_{-\infty}^{\infty} dt e^{iN\omega t} e^{-iS(t, t_{i0}, p_{s0}) + iN\omega t} + c.c. = \int_{-\infty}^{\infty} d\xi \cos(\frac{\chi}{6}\xi^3 \pm \Delta N\omega\xi), \quad (1.158)$$

so that

$$D(N\omega) \propto \frac{2\pi}{(\chi/2)^{1/3}} Ai\left[\frac{\Delta N\omega}{(\chi/2)^{1/3}}\right], \qquad (1.159)$$

where $\chi \equiv -S'''_{ttt}(t_{r0})$ and can be estimated by $\chi \cong v(t_{r0})F_0\omega$, given that $F'_t(\chi) \cong F_0\omega$ and $F(\chi) \cong 0$. Using the asymptotic expansion of the Airy functions, we obtain simple expressions for the dipole just before and after the cut-off. Before the cut-off of the harmonic spectra (for $\Delta N < 0$), the dipole oscillates, $Ai \sim \cos(-(\Delta N\omega)^{3/2}(8/9\chi)^{1/2})$, after the cut-off, the harmonic dipole exponentially decreases, $Ai \sim \exp(-(\Delta N\omega)^{3/2}(8/9\chi)^{1/2})$. The oscillations of the harmonic dipole before the cut-off are due to the interference of the short and the long trajectories.

1.14
Appendix D: Finding saddle points for the Lewenstein model

In section 1.5 we have described how one can find all saddle point solutions in the Lewenstein model for a fixed harmonic number N. Here we present an alternative and equivalent approach of finding the saddle point solutions, i.e. solving the Eqs. (1.36,1.37,1.38), which can be used in all cases, but is particularly convenient if the Fourier transform is performed numerically. The idea is to solve the Eqs. (1.36,1.37,1.38) 'forward', i.e. to fix the grid of the real recombination times and find all the other saddle point solutions, and the corresponding harmonic number N. The recombination condition Eq. (1.38) ($p_{s,\parallel} = p' + ip''$) can be re-written as

follows:

$$\left(\Delta p' + i\Delta p''\right)^2 \;=\; 2(N\omega - I_p), \tag{1.160}$$

$$\Delta p' \;\equiv\; p' - A_0 \sin(\phi_r')\cosh(\phi_r''), \tag{1.161}$$

$$\Delta p'' \;\equiv\; p'' - A_0 \sinh(\phi_r'')\cos(\phi_r'), \tag{1.162}$$

yielding

$$\left(\Delta p'\right)^2 - \left(\Delta p''\right)^2 + 2i\Delta p'\Delta p'' = 2(N\omega - I_p). \tag{1.163}$$

Since the right-hand side of this equation is real, we obtain that $\Delta p'\Delta p'' = 0$. For above threshold harmonics $(N\omega - I_p) > 0$ and $\Delta p' \neq 0$, $\Delta p'' = 0$. For below threshold harmonics $(N\omega - I_p) < 0$ and $\Delta p' = 0$, $\Delta p'' \neq 0$. Separating the imaginary and the real parts in the Eqs. (1.36,1.37), we obtain the four equations quoted in the main text, see Eqs. (1.43,1.44,1.47,1.48). Supplementing these equations for above threshold harmonics with $\Delta p'' = 0$ yields

$$p_2 = \sinh(\phi_r'')\cos(\phi_r'), \tag{1.164}$$

and for below threshold harmonics with $\Delta p' = 0$, yielding

$$p_1 = \sin(\phi_r')\cosh(\phi_r''), \tag{1.165}$$

we obtain five equations.

For above threshold harmonics: for each fixed ϕ_r' we use the Eqs. (1.47,1.48) to express ϕ_i', ϕ_i'' via p_2 and p_1 and then we use Eq. (1.164) to exclude p_2 and substitute $\phi_i'(p_1, \phi_r'')$, $\phi_i''(p_1, \phi_r'')$ and $p_2(p_1, \phi_r'')$ into the Eqs. (1.43,1.44). Using the gradient method, we can now find the minima of the function $F = F_1^2 + F_2^2$ in the plane of p_1 and ϕ_r'' for each fixed ϕ_r'. The minima define the saddle point solutions for p_1 and ϕ_r''. Knowing p_1 and ϕ_r'', we find ϕ_i', ϕ_i'', p_2 from the Eqs. (1.47,1.48,1.164). Finally, the corresponding harmonic number can be calculated from $\left(\Delta p'\right)^2 = 2(N\omega - I_p)$, yielding $N\omega = A_0^2\left(p_1 - \sin\phi_r'\cosh\phi_r''\right)^2 / 2 + I_p$. Naturally, the harmonic number defined this way does not have to be integer.

For below threshold harmonics, the procedure is essentially the same. For each fixed ϕ_r', we use the Eqs. (1.47,1.48) to express ϕ_i', ϕ_i'' via p_2 and p_1 and then we use Eq. (1.165) to exclude p_1 and substitute $\phi_i'(p_2, \phi_r'')$, $\phi_i''(p_2, \phi_r'')$ and $p_1(p_2, \phi_r'')$ into the Eqs. (1.43 and 1.44). Using the gradient method, we can now find the minima of the function $F = F_1^2 + F_2^2$ in the plane of p_2 and ϕ_r'' for each fixed ϕ_r'. The minima define the saddle point solutions for p_2 and ϕ_r''. Knowing p_2 and ϕ_r'' we find ϕ_i', ϕ_i'', p_1 from the Eqs. (1.47,1.48,1.165). Finally, the corresponding harmonic number can be calculated from $\left(\Delta p''\right)^2 = 2(I_p - N\omega)$, yielding $N\omega = I_p - A_0^2\left(p_2 - \sinh\phi_r''\cos\phi_r'\right)^2 / 2$.

In this method, it is convenient to determine the return time ϕ_{tr}' corresponding to the threshold harmonic number $N_t = I_p/\omega$. This can be easily done, since, at the threshold, $p_2 = \sinh(\phi_r'')\cos(\phi_r')$ and $p_1 = \sin(\phi_r')\cosh(\phi_r'')$. Thus, we can use these equations together with the Eqs. (1.47,1.48) to express ϕ_i', ϕ_i'' via ϕ_r' and ϕ_r'' and then use the Eqs. (1.43,1.44) to find a minimum of the function $F = F_1^2 + F_2^2$

in the plane of ϕ'_r and ϕ''_r, representing the threshold values of ϕ'_r and ϕ''_r. Once the threshold value ϕ'_{rt} of ϕ'_r is known, one can separately implement the procedures described above for below, $\phi'_r < \phi'_{rt}$, and above, $\phi'_r > \phi'_{tr}$, threshold harmonics.

Bibliography

Baker, S., Robinson, J.S., Haworth, C.A., Teng, H., Smith, R.A., Chirila, C.C., Lein, M., Tisch, J.W.G., and Marangos, J.P. (2006) Probing proton dynamics in molecules on an attosecond time scale. *Science*, **312**, 424.

Barth, I. and Smirnova, O. (2011) Nonadiabatic tunneling in circularly polarized laser fields: Physical picture and calculations. *Phys. Rev. A*, **84**, 063 415.

Barth, I. and Smirnova, O. (2013) Nonadiabatic tunneling in circularly polarized laser fields ii: Derivation of formulas. *Phys. Rev. A*, **87**, 013 433.

Becker, W., Grasbon, F., Kopold, R., B., M.D., Paulus, G.G., and Walther, H. (2002a) Above-threshold ionization: from classical features to quantum effects. *Advances In Atomic, Molecular, and Optical Physics*, **48**, 35.

Becker, W., Grasbon, F., Kopold, R., Milosevic, D.B., Paulus, G.G., and Walther, H. (2002b) Above-threshold ionization: From classical features to quantum effects. *Adv. At. Mol. Opt. Phys.*, **48**, 36.

Bloch, C. (1957) Une formulation unifiee de la theorie des reactions nucleaires. *Nuclear Physics*, **4**, 503.

Brunel, F. (1987) Not-so-resonant, resonant absorption. *Phys. Rev. Lett.*, **59**, 52.

Brunel, F. (1990) Harmonic generation due to plasma effects in a gas undergoing multiphoton ionization in the high-intensity limit. *J. Opt. Soc. Am. B*, **7**, 521.

Corkum, P.B. (1993) Plasma perspective on strong field multiphoton ionization. *Phys. Rev. Lett*, **71**, 1994.

Corkum, P.B., Burnett, N.H., and Brunel, F. (1989) Above-threshold ionization in the long-wavelength limit. *Phys. Rev. Lett.*, **62**, 1259.

Frolov, M.V., Manakov, N.L., Pronin, E.A., and Starace, A.F. (2003) Model-independent quantum approach for intense laser detachment of a weakly bound electron. *Phys. Rev. Lett.*, **91**, 053 003.

Frolov, M.V., Manakov, N.L., Sarantseva, T.S., Emelin, M.Y., Ryabikin, M.Y., and Starace, A.F. (2009) Analytic description of the high-energy plateau in harmonic generation by atoms: Can the harmonic power increase with increasing laser wavelengths? *Phys. Rev. Lett.*, **102**, 243 901.

Gaarde, M.B., Tate, J.L., and Schafer, K.J. (2008) Macroscopic aspects of attosecond pulse generation. *J. Phys. B: At. Mol. Opt. Phys.*, **41**, 132 001.

Gallagher, T. (1988) Above-threshold ionization in low-frequency limit. *Phys. Rev. Lett.,*, **61**, 2304.

Gordon, A. and Santra, R. (2006) Three-step model for high-harmonic generation in many-electron systems. *Phys. Rev. Lett*, **96**, 073 906.

Gribakin, G.F. and Kuchiev, M.Y. (1997) Multiphoton detachment of electrons from negative ions. *Phys. Rev. A*, **55**, 3760.

Grynberg, G., Aspect, A., and Fabre, C. (2010) *Introduction to Quantum Optics: From the Semi-classical Approach to Quantized Light*, Cambridge University Press.

Haessler, S.and Caillat, J., Boutu, W., Giovanetti-Teixeira, C., Ruchon, T., Auguste, T., Diveki, Z., Breger, P., Maquet, A., Carre, B., Taieb, R., and Salieres, P. (2010) Attosecond imaging of molecular electronic wavepackets. *Nature Phys.*, **6**, 200.

Harvey, A.G., Morales, F., and Smirnova, O. (2012) The r-matrix method for attosecond

spectroscopy. *Theory of electron-molecule collisions for astrophysics, biophysics and low temperature plasmas: opportunities and challenges*, **106**, 16.

Harvey, A. and J., T. (2009) The r-matrix method for attosecond spectroscopy. *J. Phys. B*, **42**, 095 101.

Huillier, A. and Balcou, P. (1993) High-order harmonic generation in rare gases with a 1-ps 1053-nm laser. *Phys Rev Lett*, **70**, 774.

Ivanov, M.Y., Brabec, T., and Burnett, N. (1996) Coulomb corrections and polarization effects in high-intensity high-harmonic emission. *Phys. Rev. A.*, **54**, 742–745.

Kaushal, J. and Smirnova, O. (2013) Non-adiabatic coulomb effects in strong field ionisation in circularly polarised laser fields i: Ionisation rates. *arXiv preprint arXiv:1302.2609*.

Keldysh, L.V. (1965) Ionization in the field of a strong electromagnetic wave. *Sov. Phys. JETP*, **20**, 1307.

Kopold, R., Becker, W., and Milosevic, D.B. (2002) Quantum orbits: a space-time picture of intense-laser-induced processes in atoms. *Journal of Modern Optics*, **49**, 1362.

Krause, J.L., Schafer, K.J., and Kulander, K.C. (1992a) High-order harmonic generation from atoms and ions in the high intensity regime. *Phys. Rev. Lett.*, **68**, 3535.

Krause, J.L., Schafer, K.J., and Kulander, K.C. (1992b) High-order harmonic generation from atoms and ions in the high intensity regime. *Phys. Rev. Lett*, **68**, 3535.

Krausz, F. and Ivanov, F. (2009) Attosecond physics. *Rev. Mod. Phys.*, **81**, 163.

Kuchiev, M.Y. (1987) Atomic antenna. *Sov. Phys. JETP Letters*, **45**, 319.

Kuchiev, M.Y. and Ostrovsky, V.N. (1999) Quantum theory of high harmonic generation as a three-step process. *Phys Rev A*, **60**, 3111.

Kulander, K., Krause, J.L., and Schafer, K.J. (1993) *NATO ASI Series*, Plenum Press, New York and London.

Le, A.T., Lucchese, R.R., Tonzani, S., Morishita, T., and Lin, C.D. (2009) Quantitative rescattering theory for high-order harmonic generation from molecules. *Phys. Rev. A*, **80**, 013 401.

Lein, M. (2005) Attosecond probing of vibrational dynamics with high-harmonic generation. *Phys Rev Lett*, **94**, 053 004.

Lewenstein, M., Balcou, P., Ivanov, M.Y., L'Huillier, A., and Corkum, P.B. (1994) Theory of high-harmonic generation by low-frequency laser fields. *Phys. Rev. A.*, **49**, 2117.

Lin, C.D., Le, A.T., Chen, Z., Morishita, T., and Lucchese, R. (2010) Strong-field rescattering physics—self-imaging of a molecule by its own electrons. *J. Phys. B: At. Mol. Opt. Phys.*, **43**, 122 001.

Lunnemann, S., Kuleff, A., and Cederbaum, L. (2008) Ultrafast charge migration in 2-phenylethyl-n,n-dimethylamine. *Chem. Phys. Lett*, **450**, 232.

Macklin, J.J., Kmetec, J.D., and Gordon, C.L. (1993) High-order harmonic generation using intense femtosecond pulses. *Phys Rev Lett*, **70**, 766.

Mairesse, Y., Higuet, J., Dudovich, N., Shafir, D., Fabre, B., Mével, E., Constant, E., Patchkovskii, S., Walters, Z., Ivanov, M.Y., and Smirnova, O. (2010) High harmonic spectroscopy of multichannel dynamics in strong-field ionization. *Phys. Rev. Lett.*, **104**, 213 601.

Morales, F., Barth, I., Serbinenko, V., Patchkovskii, S., and O., S. (2012) Shaping polarization of attosecond pulses via laser control of electron and hole dynamics. *J. Mod. Opt.*, **59**, 1303.

Morishita, T., Le, A.T., Chen, Z., and Lin, C.D. (2008) Accurate retrieval of structural information from laser-induced photoelectron and high-order harmonic spectra by few-cycle laser pulses. *Phys. Rev. Lett*, **100**, 013 903.

Murray, R., Spanner, M., Patchkovskii, S., and Ivanov, M.Y. (2011) Tunnel ionization of molecules and orbital imaging. *Phys. Rev. Lett.*, **106**, 173 001.

Ott, C., Kaldun, A., Raith, P., Meyer, K., Laux, M., Evers, J., Keitel, C.H., Greene, C.H., and T., P. (2013) Lorentz meets Fano spectral line shapes: A universal phase and its laser control. *arXiv:1301.1454*.

Patchkovskii, S., Smirnova, O., and Spanner, M. (2012) Attosecond control of electron correlations in one-photon ionization and recombination. *J. Phys. B*, **45**, 131 002.

Patchkovskii, S., Zhao, Z., Brabec, T., and Villeneuve, D.M. (2006) High harmonic generation and molecular orbital tomography in multielectron systems:

beyond the single active electron approximation. *Phys. Rev. Lett*, **97**, 123 003.

Perelomov, A.M. and Popov, V.S. (1967) *Sov. Phys. JETP,*, **25**, 336.

Perelomov, A.M., Popov, V.S., and Terent'ev, M.V. (1966) *Sov. Phys. JETP,*, **23**, 924.

Perelomov, A.M., Popov, V.S., and Terent'ev, M.V. (1967) *Sov. Phys. JETP,*, **24**, 207.

Popov, V.S., Kuznetsov, V.P., and Perelomov, A.M. (1968) *Sov. Phys. JETP,*, **26**, 222.

Popruzhenko, S.V., Mur, V.D., Popov, V.S., and Bauer, D. (2008) Strong field ionization rate for arbitrary laser frequencies. *Phys. Rev. Lett*, **101**, 193 003.

Salieres, P., Carré, B., Le Deroff, L., Grasbon, F., Paulus, G.G., Walther, H., Kopold, R., Becker, W., Milosevic, D.B., Sanpera, A., and Lewenstein, M. (2001) Feynman's path-integral approach for intense-laser-atom interactions. *Science*, **292**, 902.

Schafer, K.J., Yang, B., DiMauro, L.F., and Kulander, K.C. (1993) Above threshold ionization beyond the high harmonic cutoff. *Phys. Rev. Lett,*, **70**, 1599.

Schafer, K., Gaarde, M.B., A., H., J., B., and Keller, U. (2004) Strong field quantum path control using attosecond pulse trains. *Phys. Rev. Lett*, **92**, 023 003.

Shafir, D., Soifer, H., Bruner, B.D., Dagan, M., Mairesse, Y., Patchkovskii, S., Ivanov, M.Y., Smirnova, O., and Dudovich, N. (2012) Resolving the time when an electron exits a tunnelling barrier. *Nature*, **485**, 343.

Smirnova, O., Mairesse, Y., Patchkovskii, S., Dudovich, N., Villeneuve, D., Corkum, P., and Ivanov, M.Y. (2009a) High harmonic interferometry of multi-electron dynamics in molecules. *Nature*, **460**, 972.

Smirnova, O., Mouritzen, A.S., Patchkovskii, S., and Ivanov, M.Y. (2007a) Coulomb–laser coupling in laser-assisted photoionization and molecular tomography. *J. Phys. B: At. Mol. Opt. Phys.*, **40**, F197.

Smirnova, O., Patchkovskii, S., Mairesse, Y., Dudovich, N., and Ivanov, M.Y. (2009b) Strong-field control and spectroscopy of attosecond electron-hole dynamics in molecules. *Proceedings of the National Academy of Sciences (PNAS)*, **106**, 16 556.

Smirnova, O., Patchkovskii, S., Mairesse, Y., Dudovich, N., Villeneuve, D., Corkum, P., and Ivanov, M.Y. (2009c) Attosecond

circular dichroism spectroscopy of polyatomic molecules. *Phys. Rev. Lett.*, **102**, 063 601.

Smirnova, O., Spanner, M., and Ivanov, M. (2007b) Anatomy of strong field ionization ii: to dress or not to dress? *J. Mod. Optics*, **54**, 1019.

Smirnova, O., Spanner, M., and Ivanov, M. (2008) Analytical solutions for strong field-driven atomic and molecular one- and two-electron continua and applications to strong-field problems. *Phys. Rev. A*, **77**, 033 407.

Sukiasyan, S.and Patchkovskii, S., Smirnova, O., Brabec, T., and Ivanov, M.Y. (2010) Exchange and polarization effect in high-order harmonic imaging of molecular structures. *Phys. Rev. A*, **82**, 043 414.

Torlina, L., Ivanov, M., Walters, Z.B., and Smirnova, O. (2012) Time-dependent analytical r-matrix approach for strong-field dynamics. ii. many-electron systems. *Phys. Rev. A*, **86**, 043 409.

Torlina, L., Kaushal, J., and Smirnova, O. (2013) Nonadiabatic coulomb effects in strong field ionization in circularly polarized laser fields ii: Photoelectron spectra. *in preparation*.

Torlina, L. and Smirnova, O. (2012) Time-dependent analytical r-matrix approach for strong-field dynamics. i. one-electron systems. *Phys. Rev. A*, **86**, 043 408.

Walters, Z.B. and Smirnova, O. (2010) Attosecond correlation dynamics during electron tunnelling from molecules. *J. Phys. B: At. Mol. Opt. Phys.*, **43**, 161 002.

Weinkauf, R., Schlag, E., Martinez, T., and ., L.R. (1997) Nonstationary electronic states and site-selective reactivity. *Journal of Physical Chemistry A*, **101**, 7702.

Yudin, G.L. and Ivanov, M.Y. (2001) Nonadiabatic tunnel ionization: Looking inside a laser cycle. *Phys. Rev. A*, **64**, 013 409.

Zair, A., Holler, M., Guandalini, A., Schapper, F., Biegert, J., Gallmann, L., Keller, U., Wyatt, A.S., Monmayrant, A., Walmsley, I.A., Cormier, E., Auguste, T., Caumes, J.P., and Salières, P. (2008) Quantum path interferences in high-order harmonic generation. *Phys. Rev. Lett.*, **100**, 143 902.